Robust Intelligent Fault-Tolerant Based Finite-Time Attitude Control for Quadrotor UAV Without Angular Velocity Measurements

Kang Liu (xinxilk@mail.ustc.edu.cn)
University of Science and Technology of China https://orcid.org/0000-0003-2881-5095
Rujing Wang
Chinese Academy of Sciences Institute of Intelligent Machines

Research Article

Keywords: Angular velocity observer, Fault-tolerant attitude control, finite-time control, fuzzy logic system (FLS), neural networks (NNs).

Posted Date: May 24th, 2021

DOI: https://doi.org/10.21203/rs.3.rs-516631/v1

Noname manuscript No.
(will be inserted by the editor)

Robust Intelligent Fault-Tolerant based Finite-Time Attitude Control for Quadrotor UAV without Angular Velocity Measurements

Kang Liu · Rujing Wang

Received: date / Accepted: date

Abstract This study considers the problem of finite-time attitude control for quadrotor unmanned aerial vehicles (UAVs) subject to parametric uncertainties, external disturbances, input saturation, and actuator faults. Under the strong approximation of radial basis function neural networks (RBFNN), an adaptive finite-time NN observer is first presented to obtain the accurate information of unavailable angular velocity. More importantly, an adaptive mechanism to adjust the output gain of the fuzzy logic system (FLS) is developed to avoid the selection of larger control gains, and can even work well without the prior information on the bound of the lumped disturbance. Based on the nonsingular fast terminal sliding mode manifold, a novel switching control law is designed by incorporating the adaptive FLS and fast continuous controller in order to remove the undesired chattering phenomenon and solve the negative effects induced from the parametric uncertainty, external disturbance, and actuator fault. To deal with the input saturation, an auxiliary system is constructed. The rigorous theoretical analysis is given to prove that all the signals in the closed-loop system are uniformly bounded, and tracking errors converge into bounded neighborhoods near the origin in finite time. Moreover, the issue of selecting control parameters is analyzed in detail. Last but not least, the comparative simulation results show the validity and feasibility of the proposed control framework.

Keywords Angular velocity observer · Fault-tolerant attitude control · finite-time control · fuzzy logic system (FLS) · neural networks (NNs).

Kang Liu
Intelligent Agriculture Engineering Laboratory of Anhui Province, Institute of Intelligent Machines, and Hefei Institutes of Physical Science, Chinese Academy of Sciences, Hefei 230031, China
University of Science and Technology of China, Hefei 230026, China
E-mail: xinxilk@mail.ustc.edu.cn

Rujing Wang
Intelligent Agriculture Engineering Laboratory of Anhui Province, Institute of Intelligent Machines, and Hefei Institutes of Physical Science, Chinese Academy of Sciences, Hefei 230031, China
E-mail: rjwang@iim.ac.cn

1 Introduction

During the past decade, quadrotor unmanned aerial vehicles (UAVs) have witnessed a boost and are favored solutions to be deployed in military and civil fields, for instance, aviation reconnaissance, package delivery, aerial photography, agricultural production, wildlife protection, and so on [1–4]. In the process of such tasks, the high-performance attitude control is a significant part [5, 6]. Compared with conventional aircraft, the quadrotor possesses some specific properties such as simple structure, vertical takeoff/landing, hovering capability, and agile operation in the cluttered environment. But, there are confronted with many difficulties including the multiple-input-multiple-output (MIMO), high nonlinearity, under-actuation, and extremely complicated atmosphere, and the quadrotor system is sensitive to several uncertainties and/or disturbances [7]. Apart from increasing the challenge of the controller design, the foregoing factors pose multiple handicaps in the stable response and task success. To this end, it is imperative to develop a reliable flight framework in the control community.

Recently, several advanced control strategies are developed, such as adaptive control, sliding mode control (SMC), neural network (NN), fuzzy logic system (FLS),

Table 1 Performance comparison of various SMC methods

Comparison \ Methods	Traditional SMC	High-order SMC	Terminal SMC
Relative degree	1	$k,\ (k>1)$	1
Sliding surface	linear and/or non-linear	linear and/or non-linear	power fractional
Dimension of sliding surface	$n-1$	$n-k$	$n-1$
Convergence of sliding surface	monotone convergence	non-monotone convergence	monotone convergence
Design complexity	simple	complex	complex
Chattering degree	1.27×10^{-4}	4.81×10^{-4}	1.24×10^{-6}
Robust performance	strong	strong	strong
Strengths	Simple structure, easy design and application, appropriate to complex systems and various observers	continuous control signals, suitable for physical systems with output signals disturbed by high-level noises	finite-time convergence on sliding surface, fast dynamical response, and high-accuracy tracking phenomenon
Weaknesses	asymptotically convergence on the sliding surface, serious chattering phenomenon, and big tracking error	non-monotone convergence on the sliding surface, complex design, and large overshoot	complex computation due to control term with fractional power, slow convergence rate, and singularity problem

and the references therein. For a review of literature, an immersion and invariance-based adaptive controller was proposed in [2,8] to estimate the parametric uncertainty, without requiring a linear parameterization assumption. Despite the provision of fast response, easy implementation, and preferable robustness, SMCs have to select sufficiently large sliding gains for compensating the lumped uncertainty, and/or need a prior knowledge for the upper bound of lumped uncertainty [9,10]. However, this is unrealistic for the complexity of system uncertainty and could cause more energy loss and system chattering. For solving these problems to enhance the SMC performance, an adaptive SMC-based observer was widely applied in the recent stage [11–13]. In the work of [14], a high-order SMC is comprehensively discussed and analyzed. In [15], a novel high-order SMC strategy was proposed to address a class of arbitrary order sliding mode systems with mismatched terms. Attributed to the strong nonlinear approximation ability, the quadrotor system shows evident inhibition effects for various uncertainties [3]. In [16], an improved NN with slight online computational load is presented to avoid the explosion of online learning parameters. Due to the possibility to convey the ambiguity of human knowledge, FLS as an alternative intelligent policy is in a position to cope with the unknown nonlinearity and can provide an excellent performance. As pointed out in [17], the explosion trouble existing in the traditional backstepping method is solved by designing the adaptive fuzzy dynamic surface control. The fuzzy SMC was proposed to tackle disturbances with the chattering avoidance [18, 19]. In this way, one can gain the extra benefit that accuracy physical model and prior information of disturbances are unnecessary. Despite the advantages of the above-mentioned approaches, integrating the adaptive technique into a hybrid system including SMC, NN and FLS may destroy the stability of the whole system. In this setting, there still remains an open challenging to design a more efficient scheme without sacrificing robust performance.

Now along with the development of the control theory and the increasing demand for the high-performance tracking control, the finite-time control strategy has attracted extensive attention from researchers and engineers [6, 8, 13, 20, 21]. Its major merit is that the system state can converge to the equilibrium point after finite time rather than asymptotic convergence. To list a few, an adaptive multivariable finite-time control method was skillfully constructed in [8] to overcome the overestimation phenomenon and unknown disturbance. In [21, 22], a finite-time disturbance observer was proposed to remove the negative effects from compound disturbances. As given in [23, 24], terminal sliding mode control (TSMC), which adopts nonlinear surfaces to take the place of linear surfaces, was utilized to obtain a finite-time convergence, better transient response, and higher tracking precision. As shown in Table 1, the performance comparison of various SMC methods is given. Compared with the linear SMC, the conventional TSMC has two shortcomings that provide a slower convergence rate and exists a singularity. Therefore, the fast TSMC (FTSMC) [25–27] and nonsingular TSMC (NTSMC) [22, 28, 29] have been proposed successively. However, individual methods based on FTSMC or NTSMC can only overcome one of the above-mentioned shortcomings. Simultaneously solving two troubles, a new SMC called nonsingular FTSMC (NFTSMC) is developed and applied in different fields [21, 30–33]. However, no matter which manifold structure has a common problem in the face of the unmodeled high-frequency dynamics of output signals called the chattering phenomenon. In practical, it is particularly unexpected since it may lead to performance degradation and unforeseen instability.

To get rid of the chattering problem existing in SMCs, several solutions have been developed in succession, which can be generally divided into the following types: 1) The first solution is to employ a so-called boundary layer technique (BLT) that replaces the discontinuous term [19, 30, 31, 34], but the asymptotic stability inside the boundary layer is unable to be guaranteed, and the inadequate choice of BLT may produce large steady-state errors. 2) The second approach is to develop a continuous controller [10,23,24,33], however, it could lead to deterioration accuracy and low robustness. 3) Because the degree of the unexpected chattering is proportional to the magnitude of switching gains, some observers/approximators and adaptive approaches are designed to avoid choosing big switching gains [7, 11, 19, 20, 29, 34–36]. The afore-mentioned approaches so far solve the unwanted chattering, however, the fast finite-time nature disappears. For this important demand, it corresponds to the pursuit of our study. Moreover, most attitude control strategies for the quadrotor UAV are developed according to an idea assumption that requires the acquirability of the attitude orientation and angular velocity. From the perspective of cost limitations, sensor malfunction, and implementation considerations, angular velocity measurement may be unavailable and inaccurate. Nevertheless, this is unrealistic for the practical engineering, and so it is highly desirable to realize a free angular velocity measurement. Hence far, this issue has been deeply studied in many literature [20, 26, 38–40]. For instance, a learning observer-based adaptive algorithm was constructed to approximate the feedback velocity, which helps reduce the number of equipped sensors [26]. It has also been indicated that from the work [38], the extended state observer can accomplish the evident inhibition effects for various disturbances. In spite of that, the lumped uncertainty and its derivative require to be bounded together, and the finite-time property fails to realize. In [39], a saturated robust controller with only position measurement is proposed for a class of the motion system to overcome the problems of unknown friction, parametric uncertainty and actuator saturation. In addition to the aforesaid approaches, different finite-time observers are introduced in [20, 40] as well, however the parameter uncertainty is not considered for the design of velocity observer. As we know, the rapid and precise reconstruction of angular velocity is very important for timely accommodation of fault and saturation; otherwise, it could cause system instability, even worse, catastrophic accidents.

As a matter of fact, due to environmental changes, unexpected problems such as actuator faults and input saturation may happen at any time, especially in a sudden moment and a long-duration flight. These problems could lead to mechanical failure, large energy consumption, and unpredictable motion. Currently, research results corresponding to the input saturation mainly focus on three aspects: 1) The use of small-gain method is to reduce the input amplitude [21, 39, 41]. 2) The use of smooth function is to approximate the saturation function [42]. 3) The use of an auxiliary system is to compensate for the saturation region [43–45]. Despite these efforts, the issues concerning the strong robustness, fast anti-saturation speed, and avoidable approximation/compensation errors have to face. Moreover, the great majority of present conclusions may end up with performance degradation under actuator faults. In general, fault-tolerant control (FTC) methods can be mainly classified into two categories, that is, passive FTC (PFTC) [19, 28, 33, 46, 47] and active FTC (AFTC) [48]. Compared with the AFTC, PFTC has the ability to overcome the adverse influence of actuator faults quicker, and adapt to complex structures and real-time performance, because the feedback information from the fault diagnosis observer is needless. In this respect, this brief takes a lot of effort on PFTC for the quadrotor attitude control. The existence of two risk factors cause the attitude control problem to be more difficult and intricate. This is also another intention of our study.

Motivated by the remarkable importance and advantages, this study concentrates on designing a reliable attitude control scheme for the quadrotor UAV. Since the information of angular velocity can not be obtained directly, an adaptive finite-time NN observer (AFTNNO) is firstly constructed. By borrowing advantages from the NFTSM surface, a continuous attitude controller is developed to achieve the fast finite-time convergence, fault avoidance, and chattering attenuation. Since the upper bounds of time-varying disturbances, unknown uncertainties, and actuator faults are difficult to obtain precisely, a novel compensation term as a part of the switching controller is applied with the help of the adaptive algorithm and FLS. Additionally, an auxiliary system is developed to address the input saturation. By comparing previous conclusions comprehensively, the main contribution can be summarized as the following threefold:

1) The attitude control scheme designed in this study does not require the measurement of the angular velocity. Hence, the cost related to the velocity measurement sensors can be reduced for the controller development. Moreover, this study considers more complex situations, such as the external disturbance, parametric uncertainty, input saturation, and actuator fault, which makes the designed algorithm more

available for practical implementation. Other similar studies in [1–5, 7, 8, 13, 17–19, 19–22, 38, 39, 48] either demand the measurement of the angular velocity or only consider one of these circumstances.

2) As an alternative strategy to eliminate the chattering phenomenon and compensate for the effect of the lumped disturbance, this study presents a novel adaptive fuzzy-based fast switching controller, and which not only guarantees the finite-time stability with fast convergence speed and high tracking precision, but also does not require a stringent assumption that the lumped disturbance and its derivative are both bounded by a constant [8, 13, 21, 22, 27–29, 44]. This signifies that the proposed control scheme provides a widespread potential for application. In addition, the auxiliary design system is designed to deal with the problem of input saturation under the premise of finite-time stability.
3) Compared with existing observer techniques [20, 26, 27, 38–40, 49–51], the velocity observer is developed based on the adaptive NN technique, which can not only achieve the fast finite-time error convergence but also accurately estimate the information of angular velocity. It is worth mentioning that all the tracking signals in the closed-loop system are uniformly bounded and tracking errors can converge into small neighborhoods of the origin after a finite time. To further guarantee the practicability of the developed controller, several guidelines about the parameter adjusting are given in detail. This is very helpful for engineers to accomplish a high-precision attitude tracking of quadrotor UAV in real.

The rest of this paper is laid out in the following manner: Section 2 describes some helpful notations and preliminaries including the model of quadrotor UAV, actuator fault and saturation analysis, NN approximations, FLS, and the control objective. Next, Section 3 details the development of the angular velocity observer and attitude controller design, and gives the relevant stability analysis. Section 5 provides simulations to illustrate the effectiveness of control scheme, followed by conclusive statements and future works in Section 6.

2 Notations and Preliminaries

2.1 Notations

Throughout this work, some notations are imposed. $\mathbb{R}^n$ and $\mathbb{R}^{n\times m}$ express the $n-$ dimensional Euclidean space and $n\times m$ real matrix, respectively. $\boldsymbol{I}_n$ denotes a $n\times n$ identity matrix. $|\cdot|$ and $\|\cdot\|$ are the absolute value of a scalar and the Euclidean norm of a vector, respectively, while $\mathrm{diag}\{\bullet\}$ and $\mathrm{tr}(\bullet)$ are the diagonal matrix and the trace of a matrix, respectively. $\bar{\lambda}(\bullet)$ and $\underline{\lambda}(\bullet)$ indicate the maximum and minimum singular values of a matrix, respectively. For a given vector $\boldsymbol{y}=[y_1,y_2,y_3]^T$, a superscript $\times$ is a transformation of $\boldsymbol{y}$ to skew-symmetric matrix, i.e., $[\boldsymbol{y}]_\times=[0,-y_3,y_2;y_3,0,-y_1;-y_2,y_1,0]$.

2.2 Definitions and Lemmas

Definition 1: For any real number y, we define the hyperbolic tangent function (HTF), as follows:

$$\tanh(y):=\frac{e^{y}-e^{-y}}{e^{y}+e^{-y}}.$$

Then, for any vector $\boldsymbol{y}=[y_1,\cdots,y_n]^T$, $\tanh(\boldsymbol{y})\in\mathbb{R}^n$ can be defined as $\tanh(\boldsymbol{y})=[\tanh(y_1),\cdots,\tanh(y_n)]^T$.
Definition 2: For any given vector $\boldsymbol{x}=[x_1,\cdots,x_n]^T$ and a positive number α, we define $\mathrm{sign}(\boldsymbol{x})^\alpha\in\mathbb{R}^n$ as

$$\begin{aligned}\mathrm{sign}(\boldsymbol{x})^\alpha :=&|\boldsymbol{x}|^\alpha\mathrm{sign}(\boldsymbol{x})\\ =&\big[|x_1|^\alpha\mathrm{sign}(x_1),\ldots,|x_n|^\alpha\mathrm{sign}(x_n)\big]^T\end{aligned}$$

which can be proved that $\frac{d}{dt}(\mathrm{sign}(\boldsymbol{x})^\alpha)=\alpha|\boldsymbol{x}|^{\alpha-1}\dot{\boldsymbol{x}}$ with $\alpha\geq 1$. Moreover, we define $\mathrm{sign}(x_i)$ as

$$\mathrm{sign}(x_i):=\begin{cases}-1, & x_i<0\\ 0, & x_i=0\\ 1, & x_i>0\end{cases}.$$

In order to improve the readability of this article, we define the power of a vector $\boldsymbol{x}\in\mathbb{R}^n$, as follows:

$$\begin{aligned}\boldsymbol{x}^m :=&[x_1^m,\cdots,x_n^m]^T\in\mathbb{R}^n,\\ \dot{\boldsymbol{x}}^m :=&[\dot{x}_1^m,\cdots,\dot{x}_n^m]^T\in\mathbb{R}^n,\\ |\boldsymbol{x}|^m :=&\mathrm{diag}\{|x_1|^m,\cdots,|x_n|^m\}\in\mathbb{R}^{n\times n},\\ |\dot{\boldsymbol{x}}|^m :=&\mathrm{diag}\{|\dot{x}_1|^m,\cdots,|\dot{x}_n|^m\}\in\mathbb{R}^{n\times n}.\end{aligned}$$

Definition 3 [6]: Consider a nonlinear system as

$$\dot{\boldsymbol{x}}=f(\boldsymbol{x},\boldsymbol{u}),\ f(\boldsymbol{0},\boldsymbol{0})=\boldsymbol{0},\ \boldsymbol{x}\in\mathbb{R}^n,\ \boldsymbol{u}\in\mathbb{R}^m \tag{1}$$

wherein $\boldsymbol{x}$ and $\boldsymbol{u}$ are state and input vectors, respectively, and $f:\boldsymbol{W}\to\mathbb{R}^n$ is continuous on an open neighbourhood $\boldsymbol{W}$. The equilibrium $\boldsymbol{x}=\boldsymbol{0}$ is practical finite-time stable for the given initial condition $\boldsymbol{x}(t_0)$ with t_0 denoting the initial time, there exist $\epsilon>0$ and $T(\epsilon,\boldsymbol{x}(t_0))<\infty$ such that $\|\boldsymbol{x}(t)\|<\epsilon$ for $t\leq t_0+T$.
Lemma 1 [52]: For any two matrices $\boldsymbol{P}$ and $\boldsymbol{Q}$ that have the appropriate dimensions, it follows that $2\boldsymbol{P}^T\boldsymbol{Q}\leq\beta\boldsymbol{P}^T\boldsymbol{P}+\beta^{-1}\boldsymbol{Q}^T\boldsymbol{Q}$ with β being a positive scalar.
Lemma 2 [40]: For any real number $x_i\in\mathbb{R}^1$, there exists a positive scalar $h\in(0,1]$ that holds the following inequality, that is, $(\sum_{i=1}^n|x_i|)^h\leq\sum_{i=1}^n|x_i|^h\leq n^{1-h}(\sum_{i=1}^n|x_i|)^h$.

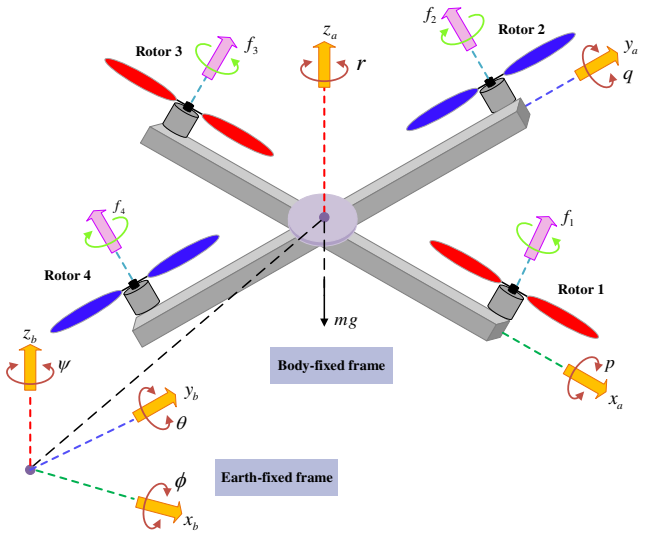

Fig. 1 Schematic configuration of a quadrotor UAV.

Lemma 3 [53]: For the nonlinear system described by (1), there is a Lyapunov function $V(t)$ holding $\dot{V}(x) \leq -\pi_1 V(x) - \pi_2 V^{\pi_3}(x) + \eta,\ \forall t > T_0$ with $0 < \eta < \infty$. Then, the trajectory of (1) is the practical finite-time stable and its solution converges to the bounded region $\Omega = \{V(x)|V(x) \leq \min\{\frac{\eta}{(1-\epsilon)\pi_1}, (\frac{\eta}{(1-\epsilon)\pi_2})^{1/\pi_3}\}\}$, where $0 < \epsilon < 1$. The convergent time T can be computed by $T \leq \max\{t_0 + \frac{1}{\epsilon\pi_1(1-\pi_3)} \ln \frac{\epsilon\pi_1 V^{1-\pi_3}(t_0)+\pi_2}{\pi_2}, t_0 + \frac{1}{\pi_1(1-\pi_3)} \ln \frac{\pi_1 V^{1-\pi_3}(t_0)+\epsilon\pi_2}{\epsilon\pi_2}\}$.

Lemma 4 [30]: For a Gauss' hypergeometric function:

$$\Lambda(\chi_1, \chi_2, \chi_3, \chi_4) = \sum_{k=0}^{\infty} \frac{(\chi_1)_k (\chi_2)_k}{(\chi_3)_k k!} \chi_4^k$$

if χ_1, χ_2, and χ_3 are positive constants and satisfy the condition $\chi_3 - \chi_2 - \chi_1 > 0$, the function $\Lambda(\cdot)$ is convergent within the definition domain $\chi_4 < 0$.

Lemma 5 [25]: For any real number z, a constant ϵ_1, $0 < p < 1$, and $0 < q = \frac{q_1}{q_2} < 1$ with q_1 and q_2 denoting positive odd integers, the following inequality is valid:

$$-z(z+\epsilon_1)^q \leq -\frac{1-p}{1+q} z^{1+q} + \frac{\epsilon_2}{1+q} \tag{2}$$

where $\epsilon_2 = \epsilon_1 + \left(\frac{\epsilon_1}{1-(1-p)^{\frac{1}{1+q}}}\right)^{1+q} + \left(\frac{\epsilon_1(1-p)^{\frac{1}{1+q}}}{1-(1-p)^{\frac{1}{1+q}}}\right)^{1+q}$.

2.3 System Description

The schematic configuration of a quadrotor UAV with the structure of symmetrical and rigid is vividly shown in Fig. 1, where the coordinate frames $\mathcal{A} = \{O_a, x_a, b_a, z_a\}$ and $\mathcal{B} = \{O_b, x_b, y_b, z_b\}$ are the earth frame with respect to the ground and the boy frame attached to the quadrotor UAV, respectively. The attitude motion for the quadrotor UAV can be controlled by adjusting the rotation speeds of four rotors appropriately. The attitude angle vector is denoted as $\boldsymbol{\Theta} = [\phi, \theta, \varphi]^T$ in the frame $\mathcal{A}$, while $\boldsymbol{\Omega} = [p_b, q_b, r_b]^T$ is the angular velocity vector in the frame $\mathcal{B}$. The relationship between $\boldsymbol{\Theta}$ and $\boldsymbol{\Omega}$ can be described in the form of

$$\boldsymbol{\Omega} = \boldsymbol{R}_s(\boldsymbol{\Theta})\dot{\boldsymbol{\Theta}} \tag{3}$$

where the rotation matrix $\boldsymbol{R}_s(\boldsymbol{\Theta})$ and its inverse matrix $\boldsymbol{R}_t(\boldsymbol{\Theta})$ are respectively written as follows:

$$\boldsymbol{R}_s = \begin{bmatrix} 1 & S_\phi T_\theta & C_\phi T_\theta \\ 0 & C_\phi & -S_\phi \\ 0 & S_\phi/C_\theta & C_\phi/C_\theta \end{bmatrix}, \boldsymbol{R}_t = \boldsymbol{R}_s^{-1} = \begin{bmatrix} 1 & 0 & -S_\theta \\ 0 & C_\phi & S_\phi C_\theta \\ 0 & -S_\phi & S_\phi C_\theta \end{bmatrix}$$

where $S_{(\cdot)} \triangleq \sin(\cdot)$, $C_{(\cdot)} \triangleq \cos(\cdot)$, and $T_{(\cdot)} \triangleq \tan(\cdot)$.

Using the Euler-Lagrangian methodology, the dynamics equation for the quadrotor attitude system can be expressed as (see among others [2,7,18])

$$\boldsymbol{J}\dot{\boldsymbol{\Omega}} = -[\boldsymbol{\Omega}] \times \boldsymbol{J}\boldsymbol{\Omega} + \boldsymbol{u} + \boldsymbol{d} \tag{4}$$

where $\boldsymbol{u} = [u_1, u_2, u_3]^T$ and $\boldsymbol{J} = \text{diag}\{J_x, J_y, J_z\}$ denote the control input and the inertial matrix, respectively; $\boldsymbol{d}$ is the lumped disturbance including the uncertain inertial matrix, external disturbance, aerodynamic friction and gyroscopic effect. Suppose that the rotor thrust is proportional to the square of the rotational speed of the rotor, that is, $u_i = \kappa_a w_i^2$, $(i = 1, 2, 3, 4)$, where $\kappa_a > 0$ and w_i are the lift coefficient and the rotary speed of the i rotor, respectively. The relationship between the rotor speed w_i and the control input u_i can be expressed by using the following matrix manner as

$$\begin{bmatrix} u_1 \\ u_2 \\ u_3 \end{bmatrix} = \begin{bmatrix} 0 & l_d\kappa_a & 0 & -l_d\kappa_a \\ -l_d\kappa_a & 0 & l_d\kappa_a & 0 \\ \kappa_b & -\kappa_b & \kappa_b & -\kappa_b \end{bmatrix} \begin{bmatrix} w_1^2 \\ w_2^2 \\ w_3^2 \\ w_4^2 \end{bmatrix} \tag{5}$$

where $\kappa_b > 0$ is the drag factor; l_d is the distance between an equipped rotor and the center of the mass.

Before proceeding, some mild assumptions are given in the subsequent development.

Assumption 1 To prevent the high-frequency oscillations of motion states, the desired attitude command $\boldsymbol{\Theta}_d$, and its time derivatives (i.e., $\dot{\boldsymbol{\Theta}}_d$ and $\ddot{\boldsymbol{\Theta}}_d$) are assumed to be bounded.

Assumption 2 To avoid the singularity at $\theta = \pm\frac{\pi}{2}$ and guarantee that the quadrotor never be overturned, angles ϕ and θ are both limited to $|\phi| < \frac{\pi}{2}$ and $|\theta| < \frac{\pi}{2}$.

Assumption 3 Due to the deployment of sensors, the structural flexibility, the variations in payloads, and other factors, the inertial matrix $\boldsymbol{J}$ is uncertain for the controller design. Thus, suppose that $\boldsymbol{J}$ is represented as $\boldsymbol{J} = \boldsymbol{J}_0 + \boldsymbol{J}_\Delta$, where $\boldsymbol{J}_0 = [J_{0,x}, J_{0,y}, J_{0,z}]^T$ is the

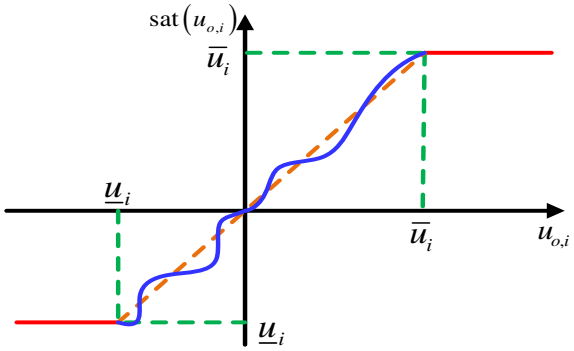

Fig. 2 Non-symmetric input saturation.

known nominal part of $\boldsymbol{J}$, and $\boldsymbol{J}_\Delta = [J_{\Delta,x}, J_{\Delta,y}, J_{\Delta,z}]^T$ regarded as the corresponding uncertain part of $\boldsymbol{J}$ is bounded such that $\|\boldsymbol{J}_\Delta\| \leq \bar{J}$ with $\bar{J}$ being an unknown positive constant.

2.4 Actuator Fault and Saturation Analysis

In the presence of actuator fault and input saturation, the output torque of ith rotor can be expressed as

$$\boldsymbol{u} = \boldsymbol{E}\text{sat}(\boldsymbol{u}_o) + \boldsymbol{u}_f \tag{6}$$

where $\boldsymbol{u}_o = [u_{o,1}, u_{o,2}, u_{o,3}]^T$ and $\boldsymbol{u}_f = [u_{f,1}, u_{f,2}, u_{f,3}]^T$ with $|u_{f,i}| < \infty$ stand for the commanded control input to be designed and additive actuator fault, respectively, while $\boldsymbol{E} = \text{diag}\{e_1, e_2, e_3\}$ with $0 < e_i \leq 1$ denotes the actuation effectiveness matrix. On this basis, there has four conditions:

(1) For $e_i = 1$ and $u_{f,i} = 0$, it indicates the fault-free condition;
(2) For $0 < e_i < 1$ and $u_{f,i} = 0$, it indicates the loss-of-effectiveness fault;
(3) For $e_i = 1$ and $u_{f,i} \neq 0$, it indicates that the ith actuator has the bias fault;
(4) For $e_i = 0$ and $u_{f,i} \neq 0$, it indicates that the ith actuator occurs the stuck fault.

In this paper, the above conditions are taken into account, except the condition (4). For the stuck fault, it often requires that the number of actuators is more than that of control outputs, and the control allocation scheme should be further investigated.

As shown in Fig. 2, the actual control input sat$(u_{o,i})$ satisfies the non-symmetric input saturation, which is described as below:

$$\text{sat}(u_{o,i}) = \begin{cases} \underline{u}_i, & u_{o,i} < \underline{u}_i \\ u_{o,i}, & \underline{u}_i \leq u_{o,i} \leq \bar{u}_i \\ \bar{u}_i, & u_{0,i} > \bar{u}_i \end{cases} \tag{7}$$

where $\underline{u}_i < 0$ and $\bar{u}_i > 0$ represent the known lower and upper bounds on $u_{o,i}$, respectively.

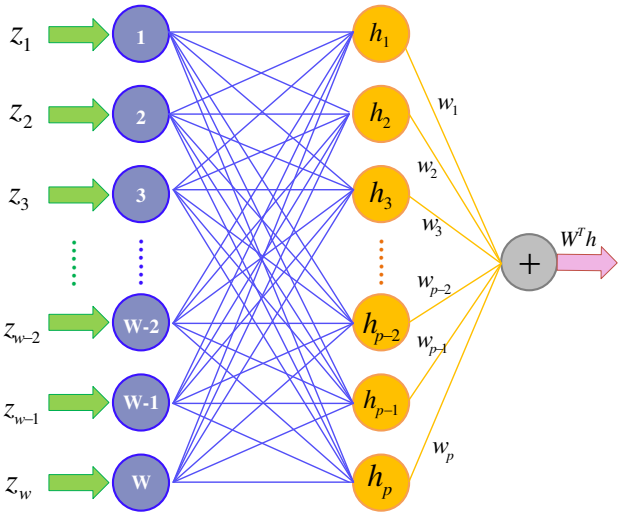

Fig. 3 Description of the architecture of the RBFNN used in this study, where the grey circle is the output of the RBFNN, the orange circle is the output of the hidden layer, and the blue circle is the input of the RBFNN.

According to previous modeling processes and Assumptions 1-3, the complete attitude equation of the quadrotor UAV is transformed into the following form

$$\boldsymbol{M}_1(\boldsymbol{\Theta})\ddot{\boldsymbol{\Theta}} + \boldsymbol{M}_2(\boldsymbol{\Theta}, \dot{\boldsymbol{\Theta}})\dot{\boldsymbol{\Theta}} = \boldsymbol{R}_t^T \boldsymbol{E}\text{sat}(\boldsymbol{u}_0) + \boldsymbol{D} \tag{8}$$

where $\boldsymbol{M}_1(\boldsymbol{\Theta}) = \boldsymbol{R}_t^T \boldsymbol{J}_0 \boldsymbol{R}_t$, $\boldsymbol{M}_2(\boldsymbol{\Theta}, \dot{\boldsymbol{\Theta}}) = \boldsymbol{R}_t^T \boldsymbol{J}_0 \dot{\boldsymbol{R}}_t - \boldsymbol{R}_t^T [\boldsymbol{J}_0 \boldsymbol{R}_t \dot{\boldsymbol{\Theta}}]_\times \boldsymbol{R}_t$ and $\boldsymbol{D} = \boldsymbol{R}_t^T (\boldsymbol{d} + \boldsymbol{J}_\Delta \boldsymbol{R}_t + \boldsymbol{J}_\Delta \dot{\boldsymbol{R}}_t - [\boldsymbol{J}_\Delta \boldsymbol{R}_t \dot{\boldsymbol{\Theta}}]_\times \boldsymbol{R}_t + \boldsymbol{u}_f)$.

Assumption 4 The lumped uncertainty $\boldsymbol{D}$ exists an unknown upper bounded $\bar{D}$ satisfying $\|\boldsymbol{D}\| \leq \bar{D}$.

Remark 1 Since the nature flight environment is constantly changing and has finite energy, the external disturbance $\boldsymbol{d}$ acting on the quadrotor UAV can be regarded as the unknown time-varying yet bounded command. Based on the definition of $\boldsymbol{R}_t$ and the recall of Assumptions 2 and 3, it is hence reasonable to give Assumption 4. Compared with the existing conclusions given in [8–10, 13, 21, 22, 27–29, 44], where $\boldsymbol{D}$ and $\dot{\boldsymbol{D}}$ are both bounded or $\dot{\boldsymbol{D}}$ is the steady-state vanishing type, this work just needs that the upper bound of $\boldsymbol{D}$ exists. Thus, Assumption 4 is also very loose and more general.

2.5 RBFNN Approximation

Since RBFNN can accurately approximate any nonlinear function, it has been extensively employed to achieve high-performance control for complex nonlinear systems. As a consequence, the smooth nonlinear function $\mathcal{F}(\boldsymbol{Z}) : \mathbb{R}^w \to \mathbb{R}$ can be approximated by

$$\mathcal{F}(\boldsymbol{Z}) = \boldsymbol{W}^{*T} \boldsymbol{h}(\boldsymbol{Z}) + \delta(\boldsymbol{Z}) \tag{9}$$

where $\boldsymbol{Z} = [z_1, \ldots, z_w]^T \in \Omega_Z \subset \mathbb{R}^w$ denotes the input vector of the RBFNN with w being the input number of RBFNN; $\delta(\boldsymbol{Z})$ signifies the function approximation error; $\boldsymbol{h}(\boldsymbol{Z}) = [h_1(\boldsymbol{Z}), \ldots, h_p(\boldsymbol{Z})] \in \mathbb{R}^p$ is the output of the hidden layer, where p is the number of neural nodes and $h_i(\boldsymbol{Z})$ is the Gaussian function defined as

$$h_i(\boldsymbol{Z}) = \exp\left(- \frac{\|\boldsymbol{Z} - \boldsymbol{C}\|^2}{\kappa^2} \right) \tag{10}$$

where $\boldsymbol{C} = [c_1, \ldots, c_w]^T \in \mathbb{R}^w$ and $\kappa \in \mathbb{R}^1$ are the center and width of the Gaussian function, respectively. $\boldsymbol{W}^* = [w_1^*, \ldots, w_p^*] \in \mathbb{R}^p$ denotes an optimal weight vector of $\boldsymbol{W} = [w_1, \ldots, w_p] \in \mathbb{R}^p$ that minimizes $\|\delta(\boldsymbol{Z})\|$ for the input $\boldsymbol{Z}$, which can be calculated by the following formulation

$$\boldsymbol{W}^* = \arg \min_{\boldsymbol{W} \in \mathbb{R}^p} \left\{ \sup_{Z \in \Omega_Z} \left| \boldsymbol{W}^T \boldsymbol{h}(\boldsymbol{Z}) - \delta(\boldsymbol{Z}) \right| \right\} \tag{11}$$

Remark 2 With respect to the RBFNN, here are three aspects that need to be stated: (i) In practice, $\boldsymbol{W}^*$ is unknown and needs to be estimated by designing the neural estimator [36] or adaptive algorithm [16], which is constrained by a positive constant $\bar{W}$, that is, $\|\boldsymbol{W}^*\| \leq \bar{W}$; (ii) Because the function $\exp(\cdot)$ is a monotonically increasing and $-\|\boldsymbol{Z} - \boldsymbol{C}\|^2 \leq 0$, there is a positive constant $\bar{h}$ such that $\|\boldsymbol{h}(\boldsymbol{Z})\| \leq \bar{h}$. (iii) In the light of *Stone-Weierstrass theorem*, one can get an uniform result that $\delta(\boldsymbol{Z})$ holds $\delta(\boldsymbol{Z}) \leq \bar{\delta}$ with $\bar{\delta}$ being a positive constant. For a more visual display, the simplified structure of the RBFNN employed in this study is shown in Fig. 3.

2.6 FLS Design

In this work, we design a FLS to handle the lumped disturbance. The fuzzy inference engine utilizes a set of fuzzy IF-THEN rules to perform a mapping from an input vector $\boldsymbol{V} = [v_1, \ldots, v_n]^T \in \mathbb{R}^n$ to an output vector $\boldsymbol{F} = [f_1, \ldots, f_n]^T \in \mathbb{R}^n$. The fuzzy linguistic rule base about the membership functions of $\boldsymbol{V}$ and $\boldsymbol{F}$ can be described in the sense that

- v_i [antecedent proposition]: P (positive), N(negative), Z (zero);
- f_i [consequent proposition]: PE (positive effect), NE (negative effect), ZE (zero effect).

The fuzzy linguistic rule base is described as follows:

- Rule 1: If v_i is P, then f_i is PE.
- Rule 2: If v_i is Z, then f_i is ZE.
- Rule 3: If v_i is N, then f_i is NE.

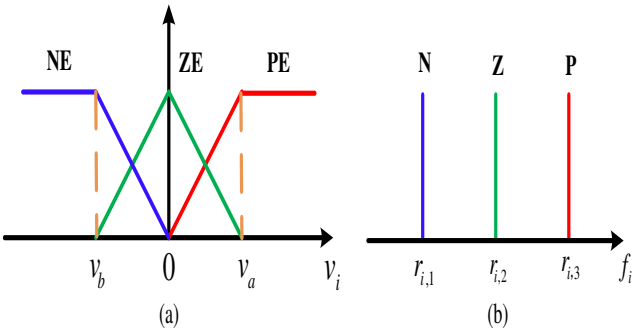

Fig. 4 Membership functions. (a) Input fuzzy sets for v_i; (b) Output fuzzy sets for f_i.

Taking account into the simple calculation and intuitive credibility, the singleton fuzzification with triangular membership functions and center of gravity defuzzification way are used accordingly. The membership functions of input and output fuzzy sets are presented in Fig. 4. The values of v_a and v_b are selected based on the system performance requirements. Thus, the output of FLS can be written as

$$\begin{aligned} f_i &= \sum_{j=1}^{3} c_j r_{ij} \Big/ \sum_{j=1}^{3} c_j \\ &= (c_1 r_{i,1} + c_2 r_{i,2} + c_3 r_{i,3})/(c_1 + c_2 + c_3) \end{aligned} \tag{12}$$

where $0 \leq c_j \leq 1$, $(j = 1, 2, 3)$, denote the firing strengths of the ith rule; $\boldsymbol{r}_a = [r_{a,1}, \ldots, r_{a,n}]^T \in \mathbb{R}^n$ represents a fuzzy vector to be selected suitably; $r_{i,1} = -r_{a,i}$, $r_{i,2} = 0$ and $r_{i,3} = r_{a,i}$ indicate the center of membership functions PE, ZE, and NE, respectively; the relation $c_1 + c_2 + c_3 = 1$ is valid in conformity to the special condition of triangular membership functions. There exists only four possible cases that need to be discussed.

- **Case 1**: Only Rule 1 is satisfied (that is, $v_i > v_a$, $c_1 = 1$, and $c_2 = c_3 = 0$), it follows that $f_i = r_{ai}$.
- **Case 2**: Both Rules 1 and 2 are satisfied (that is, $0 < v_i \leq v_a$, $0 < c_1, c_2 \leq 1$, and $c_3 = 0$), it follows that $f_i = c_1 r_{i1} = c_1 r_{ai}$.
- **Case 3**: Both Rules 2 and 3 are satisfied (that is, $v_b < v_i \leq 0$, $c_1 = 0$, and $0 < c_2, c_3 \leq 1$), it follows that $f_i = c_3 r_{i3} = -c_3 r_{ai}$.
- **Case 4**: Only Rule 4 is satisfied (that is, $v_i \leq v_b$, $c_1 = c_2 = 0$, and $c_3 = 1$), it follows that $f_i = -r_{ai}$.

Recalling the afore-mentioned Cases 1-4, it follows that $z_i(c_1 - c_3) = |z_i(c_1 - c_3)| \geq 0$. Taking a summary, one has

$$f_i = r_{a,i}(c_1 - c_3). \tag{13}$$

Control Objective: This study concentrates on designing a robust intelligent fault-tolerant based finite-time attitude controller for the quadrotor UAV with

only available attitude information, such that all the commands in the closed-loop system are ultimately uniformly bounded and tracking errors will converge into small bounded regions around the origin in finite time, despite the presence of the uncertain inertia matrix, unknown disturbances, actuator faults, and input saturation.

3 Controller Design Methodology and Stability Analysis

In this section, an adaptive finite-time NN observer (AFTNNO) is first developed to measure the angular velocity. Then, our study investigates a novel NFTSMC based adaptive FLS scheme, to eliminate the negative effects induced by the lumped uncertainty, actuator fault and the undesired chattering.

3.1 AFTNNO Design

To begin with definition of a new state variable, i.e., $\boldsymbol{w} = \dot{\boldsymbol{\Theta}}$, it follows that

$$\begin{cases} \dot{\boldsymbol{\Theta}} = \boldsymbol{w} \\ \dot{\boldsymbol{w}} = \boldsymbol{g}(\boldsymbol{\Theta}, \boldsymbol{w}) + \boldsymbol{p}_1(\boldsymbol{\Theta})\mathrm{sat}(\boldsymbol{u}_0) + \boldsymbol{p}_2(\boldsymbol{\Theta})(\boldsymbol{u}_f + \boldsymbol{d}) \end{cases} \tag{14}$$

where $\boldsymbol{g}(\boldsymbol{\Theta}, \boldsymbol{w}) = -\boldsymbol{R}_t(\boldsymbol{\Theta})\boldsymbol{J}_0^{-1}[\boldsymbol{R}_s(\boldsymbol{\Theta})\boldsymbol{w}]_\times \boldsymbol{J}\boldsymbol{R}_s(\boldsymbol{\Theta})\boldsymbol{w} - \boldsymbol{R}_t(\boldsymbol{\Theta})\boldsymbol{J}_0^{-1}\boldsymbol{J}_\Delta(\dot{\boldsymbol{R}}_s\boldsymbol{w}+\boldsymbol{R}_s\dot{\boldsymbol{w}})+\dot{\boldsymbol{R}}_t(\boldsymbol{\Theta})\boldsymbol{R}_s(\boldsymbol{\Theta})\boldsymbol{w}$, $\boldsymbol{p}_1(\boldsymbol{\Theta}) = \boldsymbol{R}_t(\boldsymbol{\Theta})\boldsymbol{J}_0^{-1}\boldsymbol{E}$, and $\boldsymbol{p}_2(\boldsymbol{\Theta}) = \boldsymbol{R}_t(\boldsymbol{\Theta})\boldsymbol{J}_0^{-1}$. It should be noticed that since the subitem $\boldsymbol{g}(\boldsymbol{\Theta}, \boldsymbol{w})$ contains the uncertain factor $\boldsymbol{J}_\Delta$, it can not be directly utilized to design the control law.

To estimate the unavailable angular velocity in the presence of the uncertain inertial matrix and other uncertain factors, we design an AFTNNO in the form of

$$\begin{cases} \dot{\hat{\boldsymbol{\Theta}}} = \hat{\boldsymbol{w}} + k_1\boldsymbol{y}_1 \\ \dot{\hat{\boldsymbol{w}}} = k_2\boldsymbol{y}_2 + \hat{\boldsymbol{W}}^{*T}\boldsymbol{h}(\boldsymbol{\Theta}, \hat{\boldsymbol{w}}) + \boldsymbol{p}_2(\boldsymbol{\Theta})\mathrm{sat}(\boldsymbol{u}_0) \end{cases} \tag{15}$$

where $\hat{\boldsymbol{\Theta}} = [\hat{\phi}, \hat{\theta}, \hat{\varphi}]^T$, $\hat{\boldsymbol{w}} = [\dot{\hat{\phi}}, \dot{\hat{\theta}}, \dot{\hat{\varphi}}]^T$ and $\hat{\boldsymbol{W}}^*$ express the estimations of $\boldsymbol{\Theta}$, $\boldsymbol{w}$ and $\boldsymbol{W}^*$, respectively. k_1 and k_2 are positive constants to be determined later. $\boldsymbol{y}_1 = \mathrm{sign}^{\frac{3l-2}{l}}(\tilde{\boldsymbol{\Theta}}) + k_3\tilde{\boldsymbol{\Theta}}$, $\boldsymbol{y}_2 = k_3\boldsymbol{y}_1 + \frac{3l-2}{l}(\mathrm{sign}^{\frac{5l-4}{l}}(\tilde{\boldsymbol{\Theta}}) + k_3\mathrm{sign}^{\frac{3l-2}{l}}(\tilde{\boldsymbol{\Theta}}))$, $\tilde{\boldsymbol{\Theta}} = \boldsymbol{\Theta} - \hat{\boldsymbol{\Theta}}$, and k_3 is a positive design constant. Here should satisfy the conditions such that $\frac{4}{5} < l < 1$ and $2l - 1 = \frac{l_1}{l_2}$, where l_1 and l_2 denote positive odd integers. In this study, $\hat{\boldsymbol{W}}^*$ can be adjusted online by using the following adaptive mechanism:

$$\dot{\hat{\boldsymbol{W}}}^* = \boldsymbol{\Upsilon}[\boldsymbol{h}(\boldsymbol{\Theta}, \hat{\boldsymbol{w}})\boldsymbol{y}_1^T - \frac{\boldsymbol{h}(\boldsymbol{\Theta}, \hat{\boldsymbol{w}})\boldsymbol{h}^T(\boldsymbol{\Theta}, \hat{\boldsymbol{w}})\hat{\boldsymbol{W}}^*}{2k_3} - k_4\hat{\boldsymbol{W}}^*] \tag{16}$$

where $\boldsymbol{\Upsilon} \in \mathbb{R}^{p\times p}$ is a positive definite matrix and $k_4 > 0$. By letting $\tilde{\boldsymbol{w}} = \boldsymbol{w} - \hat{\boldsymbol{w}}$, $\tilde{\boldsymbol{W}}^* = \boldsymbol{W}^* - \hat{\boldsymbol{W}}^*$ and $\tilde{\boldsymbol{h}} = \boldsymbol{h}(\boldsymbol{\Theta}, \boldsymbol{w}) - \boldsymbol{h}(\boldsymbol{\Theta}, \hat{\boldsymbol{w}})$, the corresponding dynamics of estimation errors can be hence derived as follows:

$$\begin{cases} \dot{\tilde{\boldsymbol{\Theta}}} = \tilde{\boldsymbol{w}} - k_1\boldsymbol{y}_1 \\ \dot{\tilde{\boldsymbol{w}}} = -k_2\boldsymbol{y}_2 + \tilde{\boldsymbol{W}}^{*T}\boldsymbol{h}(\boldsymbol{\Theta}, \hat{\boldsymbol{w}}) + \hat{\boldsymbol{W}}^{*T}\tilde{\boldsymbol{h}} + \boldsymbol{\Xi} \end{cases} \tag{17}$$

where $\boldsymbol{\Xi} = \boldsymbol{g}(\boldsymbol{\Theta}, \boldsymbol{w}) + \boldsymbol{p}_2(\boldsymbol{\Theta})(\boldsymbol{u}_f + \boldsymbol{d})$. For the sake of simplicity, we denote a new estimation error vector as $\boldsymbol{\xi} = [\boldsymbol{\xi}_1^T, \boldsymbol{\xi}_2^T]^T = [\boldsymbol{y}_1^T, \tilde{\boldsymbol{w}}]^T$. The time derivative of $\boldsymbol{\xi}$ is given by

$$\dot{\boldsymbol{\xi}} = (a\boldsymbol{A}_1 + k_3)\boldsymbol{A}_2\boldsymbol{\xi} + \boldsymbol{A}_3\Big(\tilde{\boldsymbol{W}}^{*T}\boldsymbol{h}(\boldsymbol{\Theta}, \hat{\boldsymbol{w}}) + \hat{\boldsymbol{W}}^{*T}\tilde{\boldsymbol{h}} + \boldsymbol{\Xi}\Big) \tag{18}$$

where $\boldsymbol{A}_1 = \Big[\mathrm{diag}\{|\tilde{\boldsymbol{\Theta}}|^{\frac{2l-2}{l}}\}, \boldsymbol{0}_{3\times3}; \boldsymbol{0}_{3\times3}, \mathrm{diag}\{|\tilde{\boldsymbol{\Theta}}|^{\frac{2l-2}{l}}\}\Big] \in \mathbb{R}^{6\times6}$, $\boldsymbol{A}_2 = \Big[-k_1\boldsymbol{I}_{3\times3}, \boldsymbol{I}_{3\times3}; -k_2\boldsymbol{I}_{3\times3}, \boldsymbol{0}_{3\times3}\Big] \in \mathbb{R}^{6\times6}$, $\boldsymbol{A}_3 = [\boldsymbol{0}_{3\times3}; \boldsymbol{I}_{3\times3}] \in \mathbb{R}^{6\times3}$ and $a = \frac{3l-2}{l}$. We denote $\boldsymbol{B} = \Big[\boldsymbol{I}_{3\times3}, \boldsymbol{0}_{3\times3}\Big] \in \mathbb{R}^{6\times6}$, and $\boldsymbol{E} = \boldsymbol{B}^T - \boldsymbol{C}\boldsymbol{A}_3$, where $\boldsymbol{C} \in \mathbb{R}^{6\times6}$ denotes a positive definite matrix.

In the following, the main theorem about AFTNNO is provided in details.

Theorem 1 *Consider the attitude system transformation described in (8) and the designed AFTNNO (15) and (16), under Assumptions 2-4, the estimation errors $\tilde{\boldsymbol{\Theta}}$, $\tilde{\boldsymbol{w}}$ and $\tilde{\boldsymbol{W}}^*$ will converge to small bounded regions around the origin in finite time, if the positive definite matrix $\boldsymbol{C}$ satisfies the following linear matrix inequalities (LMIs)*

$$\boldsymbol{C}\boldsymbol{A}_2 + \boldsymbol{A}_2^T\boldsymbol{C} < -\boldsymbol{K}_1 \tag{19}$$

$$\boldsymbol{C}\boldsymbol{A}_2 + \boldsymbol{A}_2^T\boldsymbol{C} + \boldsymbol{E}\boldsymbol{E}^T < -\boldsymbol{K}_2 \tag{20}$$

where $\boldsymbol{K}_1$ and $\boldsymbol{K}_2$ are arbitrarily the positive definite matrices, $k_3 > \frac{2\nu_1\bar{\lambda}(\boldsymbol{C}\boldsymbol{A}_3)^2}{\underline{\lambda}(\boldsymbol{K})_2}$ with $\nu_1 > 0$ being an arbitrary parameter, and $k_4 > \frac{\bar{h}^2}{k_3}$.

Proof: Construct the Lyapunov function as

$$V_1 = \boldsymbol{\xi}^T\boldsymbol{C}\boldsymbol{\xi} + \mathrm{tr}\{\tilde{\boldsymbol{W}}^{*T}\boldsymbol{\Upsilon}^{-1}\tilde{\boldsymbol{W}}^{*T}\} \tag{21}$$

Taking the derivative of (21) along (16) and (18), yields

$$\begin{aligned} \dot{V}_1 =& a\boldsymbol{\xi}^T\boldsymbol{A}_1(\boldsymbol{C}\boldsymbol{A}_2 + \boldsymbol{A}^T\boldsymbol{C})\boldsymbol{\xi} + k_3\boldsymbol{\xi}^T(\boldsymbol{C}\boldsymbol{A}_2 + \boldsymbol{A}^T\boldsymbol{C})\boldsymbol{\xi} \\ &+ 2\boldsymbol{\xi}\boldsymbol{C}\boldsymbol{A}_3\big[\tilde{\boldsymbol{W}}^{*T}\boldsymbol{h}(\boldsymbol{\Theta}, \hat{\boldsymbol{w}}) + \boldsymbol{W}^{*T}\boldsymbol{h} + \boldsymbol{\Xi}\big] \\ &+ k_3^{-1}\mathrm{tr}\big\{\tilde{\boldsymbol{W}}^{*T}\boldsymbol{h}(\boldsymbol{\Theta}, \hat{\boldsymbol{w}})\boldsymbol{h}(\boldsymbol{\Theta}, \hat{\boldsymbol{w}})^T\hat{\boldsymbol{W}}^{*T}\big\} \\ &+ 2k_4\mathrm{tr}\big\{\tilde{\boldsymbol{W}}^{*T}\hat{\boldsymbol{W}}^*\big\} - 2\mathrm{tr}\big\{\tilde{\boldsymbol{W}}^{*T}\boldsymbol{h}(\boldsymbol{\Theta}, \hat{\boldsymbol{w}})\boldsymbol{y}_1^T\big\}. \end{aligned} \tag{22}$$

With consideration of Lemma 5, Assumptions 3 and 4, and $\|\boldsymbol{R}_t(\boldsymbol{\Theta})\| = \frac{1}{\cos(\theta)} \le \nu_2 < \infty$, one can conclude that $\|\boldsymbol{\Xi}\| \le \|\boldsymbol{g}(\boldsymbol{\Theta}, \boldsymbol{w})\| + \|\boldsymbol{p}(\boldsymbol{\Theta})\|\|\boldsymbol{d}\| \le \bar{\delta} + \nu_2\|\boldsymbol{J}_0^{-1}\|\bar{D} \triangleq$

$\mu_{\max}$ with $\mu_{\max}$ being an unknown positive scalar. After some manipulations, (22) can be rewritten as

$$\begin{aligned}\dot{V}_1 \leq & -a\tilde{\Theta}_{\max}^{\frac{2l-2}{l}}\boldsymbol{\xi}^T\boldsymbol{K}_1\boldsymbol{\xi}+k_3\boldsymbol{\xi}^T(\boldsymbol{C}\boldsymbol{A}_2+\boldsymbol{A}^T\boldsymbol{C})\boldsymbol{\xi}\\ &+2\boldsymbol{\xi}\boldsymbol{C}\boldsymbol{A}_3\tilde{\boldsymbol{W}}^{*T}\boldsymbol{h}(\boldsymbol{\Theta},\hat{\boldsymbol{w}})+2\nu\boldsymbol{\xi}^T\lambda_{\max}^2(\boldsymbol{C}\boldsymbol{A}_3)\boldsymbol{\xi}\\ &+\nu_1^{-1}\tilde{\boldsymbol{h}}^T\boldsymbol{W}^*\boldsymbol{W}^{*T}\tilde{\boldsymbol{h}}+\nu_1^{-1}\boldsymbol{\Xi}^T\boldsymbol{\Xi}\\ &+k_3^{-1}\mathrm{tr}\{\tilde{\boldsymbol{W}}^{*T}\boldsymbol{h}(\boldsymbol{\Theta},\hat{\boldsymbol{w}})\boldsymbol{h}(\boldsymbol{\Theta},\hat{\boldsymbol{w}})^T\hat{\boldsymbol{W}}^{*T}\}\\ &+2k_4\mathrm{tr}\{\tilde{\boldsymbol{W}}^{*T}\hat{\boldsymbol{W}}^*\}-2\mathrm{tr}\{\tilde{\boldsymbol{W}}^{*T}\boldsymbol{h}(\boldsymbol{\Theta},\hat{\boldsymbol{w}})\boldsymbol{y}_1^T\}\\ \leq & -a\tilde{\Theta}_{\max}^{\frac{2l-2}{l}}\boldsymbol{\xi}^T\boldsymbol{K}_1\boldsymbol{\xi}+k_3\boldsymbol{\xi}^T(\boldsymbol{C}\boldsymbol{A}_2+\boldsymbol{A}^T\boldsymbol{C})\boldsymbol{\xi}\\ &+2\boldsymbol{\xi}\boldsymbol{C}\boldsymbol{A}_3\tilde{\boldsymbol{W}}^{*T}\boldsymbol{h}(\boldsymbol{\Theta},\hat{\boldsymbol{w}})+2\nu\boldsymbol{\xi}^T\lambda_{\max}^2(\boldsymbol{C}\boldsymbol{A}_3)\boldsymbol{\xi}\\ &+\nu_1^{-1}\bar{W}^2\bar{h}^2+\nu_1^{-1}\mu_{\max}^2\\ &+k_3^{-1}\mathrm{tr}\{\tilde{\boldsymbol{W}}^{*T}\boldsymbol{h}(\boldsymbol{\Theta},\hat{\boldsymbol{w}})\boldsymbol{h}(\boldsymbol{\Theta},\hat{\boldsymbol{w}})^T\hat{\boldsymbol{W}}^{*T}\}\\ &+2k_4\mathrm{tr}\{\tilde{\boldsymbol{W}}^{*T}\hat{\boldsymbol{W}}^*\}-2\mathrm{tr}\{\tilde{\boldsymbol{W}}^{*T}\boldsymbol{h}(\boldsymbol{\Theta},\hat{\boldsymbol{w}})\boldsymbol{y}_1^T\} \quad (23)\end{aligned}$$

where $\tilde{\Theta}_{\max}=\max\{\tilde{\Theta}_1,\tilde{\Theta}_2,\tilde{\Theta}_3\}$ and $\boldsymbol{y}_1=\boldsymbol{C}\boldsymbol{\xi}$. The use of $(0.5k_3\|\tilde{\boldsymbol{W}}^*\|^2)^{\frac{2l-1}{l}}-0.5k_3\|\tilde{\boldsymbol{W}}^*\|^2\leq 1$, $\tilde{\boldsymbol{W}}^{*T}\hat{\boldsymbol{W}}^*=\tilde{\boldsymbol{W}}^{*T}\boldsymbol{W}^*-\|\tilde{\boldsymbol{W}}^*\|^2\leq -(1/2)\|\tilde{\boldsymbol{W}}^*\|^2+(1/2)\bar{W}^2$, Lemma 5, LMI (20) and $\boldsymbol{E}=\boldsymbol{B}^T-\boldsymbol{C}\boldsymbol{A}_3$ provided earlier, (23) can be transformed to be

$$\begin{aligned}\dot{V}_1 \leq & -a\tilde{\Theta}_{\max}^{\frac{2l-2}{l}}\boldsymbol{\xi}^T\boldsymbol{K}_1\boldsymbol{\xi}+k_3\boldsymbol{\xi}^T(\boldsymbol{C}\boldsymbol{A}_2+\boldsymbol{A}^T\boldsymbol{C})\boldsymbol{\xi}\\ &-2\boldsymbol{\xi}\boldsymbol{E}\tilde{\boldsymbol{W}}^{*T}\boldsymbol{h}(\boldsymbol{\Theta},\hat{\boldsymbol{w}})+2\nu\boldsymbol{\xi}^T\lambda_{\max}^2(\boldsymbol{C}\boldsymbol{A}_3)\boldsymbol{\xi}\\ &+\nu_1^{-1}\bar{W}^2\bar{h}^2+\nu_1^{-1}\mu_{\max}^2-0.5\big(k_4-k_3^{-1}\bar{h}^2\big)\|\tilde{\boldsymbol{W}}^*\|^2\\ &-\big(0.5k_4\|\tilde{\boldsymbol{W}}^*\|^2\big)^{\frac{2l-1}{l}}-k_3^{-1}\boldsymbol{h}^T(\boldsymbol{\Theta},\hat{\boldsymbol{w}})\tilde{\boldsymbol{W}}^*\tilde{\boldsymbol{W}}^{*T}\\ &\times\boldsymbol{h}(\boldsymbol{\Theta},\hat{\boldsymbol{w}})+0.5k_3^{-1}\bar{W}^2\bar{h}^2+k_4\bar{W}^2+1\\ \leq & -a\tilde{\Theta}_{\max}^{\frac{2l-2}{l}}\lambda_{\max}(\boldsymbol{K}_1)\|\boldsymbol{\xi}\|^2-k_3\lambda_{\min}(\boldsymbol{K}_2)\|\boldsymbol{\xi}\|^2\\ &+2\nu\lambda_{\max}^2(\boldsymbol{C}\boldsymbol{A}_3)\|\boldsymbol{\xi}\|^2-0.5\big(k_4-k_3^{-1}\bar{h}^2\big)\|\tilde{\boldsymbol{W}}^*\|^2\\ &-\big(0.5k_4\|\tilde{\boldsymbol{W}}^*\|^2\big)^{\frac{2l-1}{l}}+\nu_1^{-1}\bar{W}^2\bar{h}^2+\nu_1^{-1}\mu_{\max}^2\\ &+0.5k_3^{-1}\bar{W}^2\bar{h}^2+k_4\bar{W}^2+1. \quad (24)\end{aligned}$$

Since $\frac{2l-2}{l}<0$ and $\tilde{\Theta}_{\max}\leq\|\tilde{\boldsymbol{\Theta}}\|\leq k_3^{-1}\|\boldsymbol{y}_1\|\leq k_3^{-1}\|\boldsymbol{\xi}\|$, one can get that $\tilde{\Theta}_{\max}^{\frac{2l-2}{l}}\geq\big(k_3^{-1}\|\boldsymbol{\xi}\|\big)^{\frac{2l-2}{l}}$. With the help of Lemma 2, the inequality (24) is re-expressed as

$$\begin{aligned}\dot{V}_1 \leq & -a\lambda_{\max}(\boldsymbol{K}_1)k_3^{\frac{2-2l}{l}}\|\boldsymbol{\xi}\|^{\frac{4l-2}{l}}-(0.5k_4)^{\frac{2l-1}{l}}\|\tilde{\boldsymbol{W}}^*\|^{\frac{4l-2}{l}}\\ &-\big(k_3\lambda_{\min}(\boldsymbol{K}_2)-2\nu\lambda_{\max}^2(\boldsymbol{C}\boldsymbol{A}_3)\big)\|\boldsymbol{\xi}\|^2\\ &-0.5\big(k_4-k_3^{-1}\bar{h}^2\big)\|\tilde{\boldsymbol{W}}^*\|^2+\Delta_1\\ \leq & -\Psi_1V_1-\Psi_2V_1^{\frac{2l-1}{l}}+\Delta_1 \quad (25)\end{aligned}$$

as long as $k_3>\frac{2\nu\lambda_{\max}^2(\boldsymbol{C}\boldsymbol{A}_3)}{k_3\lambda_{\min}(\boldsymbol{K}_2)}$ and $k_4>\frac{\bar{h}^2}{k_3}$, (25) will be satisfied. In (25), $\Psi_1=\min\big\{a\lambda_{\max}(\boldsymbol{K}_1)k_3^{\frac{2-2l}{l}},(0.5k_4)^{\frac{2l-1}{l}}\big\}$, $\Psi_2=\min\big\{k_3\lambda_{\min}(\boldsymbol{K}_2)-2\nu\lambda_{\max}^2(\boldsymbol{C}\boldsymbol{A}_3),0.5\big(k_4-k_3^{-1}\bar{h}^2\big)\big\}$ and $\Delta_1=\nu_1^{-1}\mu_{\max}^2+0.5k_3^{-1}\bar{W}^2\bar{h}^2+k_4\bar{W}^2+1$. In accordance with Lemma 3, it is not difficult to infer that estimation errors and tracking errors (i.e., $\tilde{\boldsymbol{\Theta}}$, $\tilde{\boldsymbol{w}}$ and $\tilde{\boldsymbol{W}}^*$) shall tend to the following bounded regions as

$$\begin{cases}\|\tilde{\boldsymbol{\Theta}}\|\leq k_3^{-1}\lambda_{\min}^{-\frac{1}{2}}(\boldsymbol{C})\min\Big\{\frac{\Delta_1}{(1-\epsilon_1)\Psi_1},\Big(\frac{\Delta_1}{(1-\epsilon_2)\Psi_1}\Big)^{l/(1-l)}\Big\}\\ \|\tilde{\boldsymbol{w}}\|\leq\lambda_{\min}^{-\frac{1}{2}}(\boldsymbol{C})\min\Big\{\frac{\Delta_1}{(1-\epsilon_1)\Psi_1},\Big(\frac{\Delta_1}{(1-\epsilon_2)\Psi_1}\Big)^{l/(1-l)}\Big\}\\ \|\tilde{\boldsymbol{W}}^*\|\leq\lambda_{\min}^{-\frac{1}{2}}(\boldsymbol{\Upsilon}^{-1})\min\Big\{\frac{\Delta_1}{(1-\epsilon_1)\Psi_1},\Big(\frac{\Delta_1}{(1-\epsilon_2)\Psi_1}\Big)^{l/(1-l)}\Big\}\end{cases} \quad (26)$$

where $0<\epsilon_1<1$. Moreover, the setting time T_1 is calculated by $T_1\leq t_0+\max\Big\{\frac{l}{\epsilon_1\Psi_1(1-l)}\ln\frac{\epsilon_1\Psi_1V_1^{(1-l)/l}(t_0)+\Psi_2}{\Psi_2},\frac{l}{\Psi_1(1-l)}\ln\frac{\Psi_1V_1^{(1-l)/l}(t_0)+\epsilon_1\Psi_2}{\epsilon_1\Psi_2}\Big\}$. Consequently, this completes proof.

Remark 3 In many existing works [1–5, 7, 13, 17], the attitude angular velocity is assumed to be measurable. This could cause these approaches to no longer useful in practical application, and thus an AFTNNO is developed in this study to tackle this challenge. Although different kinds of observers have been developed in [49–51] recently, the application of these control frameworks is required to know the accurate inertia matrix. To the best of our knowledge, the fast and accurate reconstruction of angular velocity looks forward to providing significant support for the timely solution of fault and saturation; otherwise, it is prone to task failure, even worse, serious flight accidents.

3.2 Robust Intelligent Fault-Tolerant based Finite-Time Attitude Controller Design

For the purpose of the finite-time convergence, preferable robustness, and rapid response, a NFTSM surface $\boldsymbol{s}_n=[s_{n,1},s_{n,2},s_{n,3}]^T$ containing the attitude-tracking error and angular velocity tracking error is introduced as [30, 32]

$$\boldsymbol{s}_n=\boldsymbol{\Theta}_e+\beta_a\mathrm{sign}(\boldsymbol{\Theta}_e)^{m_c}+\beta_b\mathrm{sign}(\dot{\boldsymbol{\Theta}}_e)^{\frac{m_a}{m_b}} \quad (27)$$

where β_a and β_b are positive design parameters; m_a and m_b denote positive odd integers with the relationships of $1<\frac{m_a}{m_b}<2$ and $m_c>\frac{m_a}{m_b}$. Particularly, since this study can estimate the unavailable angular velocity signal and attitude signal, $\boldsymbol{\Theta}$ and its derivative $\dot{\boldsymbol{\Theta}}$ are substituted by their estimation values $\hat{\boldsymbol{\Theta}}$ and $\dot{\hat{\boldsymbol{\Theta}}}$. From the AFTNNO in (15), the estimated tracking errors $\boldsymbol{\Theta}_e$ and $\dot{\boldsymbol{\Theta}}_e$ in (27) is hence defined as $\boldsymbol{\Theta}_e=\hat{\boldsymbol{\Theta}}-\boldsymbol{\Theta}_d$ and $\dot{\boldsymbol{\Theta}}_e=\hat{\boldsymbol{w}}-\dot{\boldsymbol{\Theta}}_d$, respectively.

Remark 4 The fast finite-time convergence for the control strategy-based NFTSM manifold is interpreted as

follows: When the system state approaches the neighborhood of the equilibrium point, the lower-order term of $\boldsymbol{\Theta}_e$ plays a leading role to ensure the faster reaching rate. During this phase, the convergence speed of the system state on the NFTSM manifold is analogous to that on the NTSM manifold described by $\dot{\boldsymbol{\Theta}}_e = -(1/\beta_b)^{m_b/m_a}\text{sign}(\boldsymbol{\Theta}_e)^{m_a/m_b}$. When the system state is far from the equilibrium state, the higher-order term of $\boldsymbol{\Theta}_e$ has a great effect on improving the convergence rate. During this phase, the convergence rate of the system state on the NFTSM manifold is quicker than that on the NTSM manifold described by $\dot{\boldsymbol{\Theta}}_e = -(\beta_a/\beta_b)^{m_b/m_a}$ $\text{sign}(\boldsymbol{\Theta}_e)^{m_a/m_b}$. By doing so, one can conclude that the system state can converge to the equilibrium state faster on the NFTSM manifold than on the NTSM manifold. In contrast to the FTSM manifold described by $\boldsymbol{s}_{FTSM} = \dot{\boldsymbol{\Theta}}_e + p_a\text{sign}(\boldsymbol{\Theta}_e)^{p_c} + p_b\text{sign}(\boldsymbol{\Theta}_e)^{p_d}$ with $p_a > 0$, $p_b > 0$, $p_c \geq 1$ and $0 < p_d < 1$, the NFTSM manifold has a merit to solve the singular problem since $m_a/m_b > 1$ can prevent any negative power induced by the derivative of $\boldsymbol{s}_n$.

To design the attitude control law, the time derivative of (27) along (8) is first formulated as

$$\begin{aligned}\dot{\boldsymbol{s}}_n =&\dot{\boldsymbol{\Theta}}_e + \beta_a m_c|\boldsymbol{\Theta}_e|^{m_c-1}\dot{\boldsymbol{\Theta}}_e + \beta_b\frac{m_a}{m_b}|\dot{\boldsymbol{\Theta}}_e|^{\frac{m_a}{m_b}-1}\\ &+ \boldsymbol{M}_1^{-1}\big(-\boldsymbol{M}_2\dot{\hat{\boldsymbol{\Theta}}} - \boldsymbol{M}_1\ddot{\boldsymbol{\Theta}}_d + \boldsymbol{R}_t^T\boldsymbol{E}\text{sat}(\boldsymbol{u}) + \boldsymbol{D}\big).\end{aligned} \tag{28}$$

Thereby, we obtain the equivalent controller $\boldsymbol{u}_{o,eq}$ by computing the equation $\dot{\boldsymbol{s}}_n = \boldsymbol{0}$ in the absence of the lumped disturbance and actuator fault.

$$\begin{aligned}\boldsymbol{u}_{o,eq} =& -\boldsymbol{P}_2\bigg(\frac{\beta_a m_c m_b}{\beta_b m_a}\text{diag}\{|\boldsymbol{\Theta}_e|^{m_c-1}\}\text{sign}(\dot{\boldsymbol{\Theta}}_e)^{2-\frac{m_a}{m_b}}\\ &+ \frac{m_a}{m_b\beta_b}\text{sign}(\dot{\boldsymbol{\Theta}}_e)^{2-\frac{m_a}{m_b}} + \boldsymbol{P}_1\dot{\hat{\boldsymbol{\Theta}}} - \ddot{\boldsymbol{\Theta}}_d\bigg).\end{aligned} \tag{29}$$

where $\boldsymbol{P}_1 = \boldsymbol{M}_1^{-1}\boldsymbol{M_2}$ and $\boldsymbol{P}_2 = \boldsymbol{M}_1^{-1}\boldsymbol{R}_t^T\boldsymbol{E}$.

Since the lumped disturbance and actuator faults are inevitable in practical engineering, the switching controller for dealing with this issue are put forward in the following manner:

$$\begin{cases}\boldsymbol{u}_{o,sw} = -\boldsymbol{P}_2^{-1}(\boldsymbol{u}_{o,sw,1} + \boldsymbol{u}_{o,sw,2})\\ \boldsymbol{u}_{o,sw,1} = k_a\boldsymbol{s}_n + k_b\text{sign}(\boldsymbol{s}_n)^{\frac{k_c}{k_d}}\\ \boldsymbol{u}_{o,sw,2} = \boldsymbol{r}_a(c_1 - c_3)\end{cases} \tag{30}$$

where k_a and k_b are positive design parameters, k_c and k_d are positive odd integers with $k_c < k_d$, and the definitions of c_1, c_3, and $\boldsymbol{r}_a$ are already given in (12).

To eliminate the negative effect from the input saturation, an auxiliary system is constructed as

$$\dot{\boldsymbol{\chi}} = -n_a\boldsymbol{\chi} - n_b\boldsymbol{\chi}^{\frac{m_a}{m_b}} - \frac{\boldsymbol{s}_n^T\boldsymbol{s}_n + \triangle\boldsymbol{u}^T\triangle\boldsymbol{u}}{2||\boldsymbol{\chi}||^2}\boldsymbol{\chi} + \triangle\boldsymbol{u} \tag{31}$$

where $\Delta\boldsymbol{u} = \boldsymbol{u}_o - \text{sat}(\boldsymbol{u})$, $n_a > 1$ and $n_b > 0$. Thus, the saturation compensation controller $\boldsymbol{u}_{o,sa}$ is designed as

$$\boldsymbol{u}_{o,sa} = \boldsymbol{P}_2^{-1}\boldsymbol{\chi}. \tag{32}$$

Recalling the pervious design development, the composite attitude controller is given by

$$\boldsymbol{u}_o = \boldsymbol{u}_{o,eq} + \boldsymbol{u}_{o,sw} + \boldsymbol{u}_{o,sa}. \tag{33}$$

Consider the following Lyapunov function as

$$V_2 = V_1 + \frac{1}{2}\boldsymbol{s}_n^T\boldsymbol{s}_n + \frac{1}{2}\boldsymbol{\chi}^T\boldsymbol{\chi}. \tag{34}$$

Substituting (33) into the time derivative of (34), and utilizing the Lemma 1 that $\boldsymbol{s}_n^T\boldsymbol{\chi} \leq \frac{1}{2}(\boldsymbol{s}_n^T\boldsymbol{s}_n + \boldsymbol{\chi}^T\boldsymbol{\chi})$ and $\boldsymbol{\chi}^T\Delta\boldsymbol{u} \leq \frac{1}{2}(\boldsymbol{\chi}^T\boldsymbol{\chi} + \Delta\boldsymbol{u}^T\Delta\boldsymbol{u})$, one can obtain that

$$\begin{aligned}\dot{V}_2 \leq&\boldsymbol{s}_n^T\Big\{\dot{\boldsymbol{\Theta}}_e + \beta_a m_c\text{diag}(|\boldsymbol{\Theta}_e|^{m_c-1})\dot{\boldsymbol{\Theta}}_e - \text{diag}(|\dot{\boldsymbol{\Theta}}_e|^{\frac{m_a}{m_b}-1})\\ &\times\big[\text{sign}(\dot{\boldsymbol{\Theta}}_e)^{2-\frac{m_a}{m_b}} - \beta_a m_c\text{diag}(|\boldsymbol{\Theta}_e|^{m_c-1})\text{sign}(\dot{\boldsymbol{\Theta}}_e)^{2-\frac{m_a}{m_b}}\\ &- \frac{\beta_b m_a}{m_b}\big(k_a\boldsymbol{s}_n + k_b\text{sign}(\boldsymbol{s}_n)^{\frac{k_c}{k_d}} - \boldsymbol{D} + \boldsymbol{r}_a(c_1 - c_3)\big)\big]\Big\}\\ &- n_a\boldsymbol{\chi}^T\boldsymbol{\chi} - n_b\boldsymbol{\chi}^T\boldsymbol{\chi}^{\frac{k_c}{k_d}} + \boldsymbol{s}_n^T\boldsymbol{\chi} - \frac{1}{2}\boldsymbol{s}_n^T\boldsymbol{s}_n - \frac{1}{2}\triangle\boldsymbol{u}^T\triangle\boldsymbol{u}\\ &+ \boldsymbol{\chi}^T\triangle\boldsymbol{u} - \Psi_1 V_1 - \Psi_2 V_1^{\frac{2l-1}{l}} + \Delta_1\\ \leq& -\frac{\beta_b m_a}{m_b}\boldsymbol{s}_n^T\text{diag}(|\dot{\boldsymbol{\Theta}}_e|^{\frac{m_a}{m_b}-1})\big(k_a\boldsymbol{s}_n + k_b\text{sign}(\boldsymbol{s}_n)^{\frac{k_c}{k_d}}\\ &- \boldsymbol{D} + \boldsymbol{r}_a(c_1 - c_3)\big) - (n_a - 1)\boldsymbol{\chi}^T\boldsymbol{\chi} - n_b\boldsymbol{\chi}^T\boldsymbol{\chi}^{\frac{k_c}{k_d}}\\ &- \Psi_1 V_1 - \Psi_2 V_1^{\frac{2l-1}{l}} + \Delta_1.\end{aligned} \tag{35}$$

According to the detailed analysis about FLS and using $\boldsymbol{s}_n$ as the input vector of FLS, it can be confirmed that $\boldsymbol{s}_n(c_1 - c_3)$ is a positive vector. Thus, we have

$$-\boldsymbol{s}_n^T\boldsymbol{r}_a(c_1 - c_3) + \boldsymbol{s}_n^T\boldsymbol{D} = -(c_1 - c_3)\boldsymbol{s}_n^T\Big(\boldsymbol{r}_a - \frac{1}{c_1 - c_3}\boldsymbol{D}\Big). \tag{36}$$

If each element of $\boldsymbol{r}_a$ satisfies $r_{ai} \geq |\frac{\bar{D}}{c_1 - c_3}|$, the inequality (35) can be transformed based on Lemma 2, as

$$\begin{aligned}\dot{V}_2 \leq& -\frac{\beta_b m_a}{m_b}\boldsymbol{s}_n^T\text{diag}(|\dot{\boldsymbol{\Theta}}_e|^{\frac{m_a}{m_b}-1})(k_a\boldsymbol{s}_n + k_b\text{sign}(\boldsymbol{s}_n)^{\frac{k_c}{k_d}})\\ &- (n_a - 1)\boldsymbol{\chi}^T\boldsymbol{\chi} - n_b\boldsymbol{\chi}^T\boldsymbol{\chi}^{\frac{k_c}{k_d}} - \Psi_1 V_1 - \Psi_2 V_1^{\frac{2l-1}{l}} + \Delta_1\\ =& -\boldsymbol{s}_n^T\boldsymbol{L}_1\boldsymbol{s}_n - \boldsymbol{s}_n^T\boldsymbol{L}_2\text{sign}(\boldsymbol{s}_n)^{\frac{k_c}{k_d}} - (n_a - 1)\boldsymbol{\chi}^T\boldsymbol{\chi}\\ &- n_b\boldsymbol{\chi}^T\boldsymbol{\chi}^{\frac{k_c}{k_d}} - \Psi_1 V_1 - \Psi_2 V_1^{\frac{2l-1}{l}} + \Delta_1\\ \leq& -\lambda_{\min}(\boldsymbol{L}_1)\boldsymbol{s}_n^T\boldsymbol{s}_n - \lambda_{\min}(\boldsymbol{L}_2)\|\boldsymbol{s}_n\|^{\frac{k_c+k_d}{k_d}} - n_b\|\boldsymbol{\chi}\|^{\frac{k_c+k_d}{k_d}}\\ &- (n_a - 1)\boldsymbol{\chi}^T\boldsymbol{\chi} - \Psi_1 V_1 - \Psi_2 V_1^{\frac{2l-1}{l}} + \Delta_1\\ \leq& -L_3 V_2 - L_4 V_2^{\frac{2l-1}{l}} + \Delta_1\end{aligned} \tag{37}$$

where $n_a > 1$, $\frac{2l-1}{l} = \frac{k_c+k_d}{2k_d}$, $\boldsymbol{L}_1 = \frac{k_a\beta_b m_a}{m_b}\mathrm{diag}(|\dot{\boldsymbol{\Theta}}_e|^{\frac{m_a}{m_b}-1})$, $\boldsymbol{L}_2 = \frac{k_b\beta_b m_a}{m_b}\mathrm{diag}(|\dot{\boldsymbol{\Theta}}_e|^{\frac{m_a}{m_b}-1})$, $L_3 = \min\{2\lambda_{\min}(\boldsymbol{L}_1), 2(n_a-1), \Psi_1\}$, and $L_4 = \min\Big\{2^{\frac{k_c+k_d}{2k_d}}\lambda_{\min}(\boldsymbol{L}_2), 2^{\frac{k_c+k_d}{2k_d}}n_b, \Psi_2\Big\}$.

From (37), one can illustrate that the system is the practical finite-time stable with the aid of Lemma 3. Since the accuracy upper bound of lumped disturbance is hard to obtain in practice, a bigger $\boldsymbol{r}_a$ needs to be chosen in order to ensure the system stability. However, it will cause even more energy loss. So as a solution to this dilemma, an adaptive algorithm is developed to adjust the parameter vector $\boldsymbol{r}_a$ online, as follows:

$$\dot{\hat{\boldsymbol{r}}}_a = \frac{\beta_b m_a}{m_b}|\dot{\boldsymbol{\Theta}}_e|^{\frac{m_a}{m_b}-1}\frac{\boldsymbol{s}_n(c_1-c_3)}{\sigma} - \mu_1\hat{\boldsymbol{r}}_a - \mu_2\hat{\boldsymbol{r}}_a^{\mu_3} \quad (38)$$

where $\hat{\boldsymbol{r}}_a = [\hat{r}_{a,1}, \hat{r}_{a,2}, \hat{r}_{a,3}]^T$, $\hat{\boldsymbol{r}}_a(0) \geq 0$, $\mu_1 > 0$, $\mu_2 > 0$, $0 < \mu_3 < 1$, and σ represents a positive constant determining the rate of the estimated bound $\hat{\boldsymbol{r}}_a$. With the aforesaid preparations, the designed control law can be deduced to

$$\begin{aligned}\boldsymbol{u}_o = -\boldsymbol{P}_2\Bigg(&\frac{\beta_a m_c m_b}{\beta_b m_a}\mathrm{diag}\{|\boldsymbol{\Theta}_e|^{m_c-1}\}\mathrm{sign}(\dot{\boldsymbol{\Theta}}_e)^{2-\frac{m_a}{m_b}}\\ &+\frac{m_a}{m_b\beta_b}\mathrm{sign}(\dot{\boldsymbol{\Theta}}_e)^{2-\frac{m_a}{m_b}} + \boldsymbol{P}_1\dot{\boldsymbol{\Theta}} - \ddot{\boldsymbol{\Theta}}_d + k_a\boldsymbol{s}_n\\ &+k_b\mathrm{sign}(\boldsymbol{s}_n)^{\frac{k_c}{k_d}} + \hat{\boldsymbol{r}}_a(c_1-c_3) - \boldsymbol{\chi}\Bigg). \end{aligned} \quad (39)$$

Remark 5 In (33), the subitem $\boldsymbol{u}_{o,eq}$ is nominal feedback control, the subitem $\boldsymbol{u}_{o,sw}$ is a fast-type reaching control to suppress the undesired chattering and guarantee strong robustness against the lumped disturbance, and the subitem $\boldsymbol{u}_{o,sa}$ as a compensation control serves for dealing with the input saturation.

Remark 6 For the previous finite-time control strategies developed in [8,13,20–22,25,27,28,31,42,47], where only part of the input saturation, actuator faults, parametric uncertainty, and external disturbance is taken into account. In this study, all these factors are considered into the controller development. Therefore, our study is of both theoretical significance and practical worth to pave the way for achieving the high-performance attitude tracking of the quadrotor UAV.

The overall block diagram for the attitude control system of the quadrotor UAV is delicately shown in Fig. 5. In the following, we are able to give the stability analysis of the closed-loop system in Theorem 2.

Theorem 2 *Consider the attitude system transformation described in (8) and Assumptions 1-4. By applying the designed controller (39) with an adaptive mechanism (38), all the signals in the closed-loop system can be guaranteed to be bounded uniformly, and tracking errors will converge to bounded regions near the origin in finite time.*

Proof: Consider the Lyapunov function as

$$V_3 = V_2 + \frac{\sigma}{2}\sum_{i=1}^{3}\tilde{r}_{a,i}^2 \quad (40)$$

where $\tilde{r}_{a,i} = \hat{r}_{a,i} - \bar{r}_{a,i}$ is the estimation error, and $\bar{r}_{a,i}$ represents an upper bound of $\hat{r}_{a,i}$. Without loss of generality, $\bar{r}_{a,i}$, $(i = 1, 2, 3)$, are suppose to be $\bar{r}_{a,i} = |\frac{\bar{D}}{c_1-c_3}| + r_{0,i}$, and in which the scalar $r_{0,i}$ is a very small positive constant and belongs to the element of $\boldsymbol{r}_o \in \mathbb{R}^3$.

Evaluating the derivative of (40) along (38) and (39), results in

$$\begin{aligned}\dot{V}_3 \leq &-\frac{\beta_b m_a}{m_b}\boldsymbol{s}_n^T\mathrm{diag}(|\dot{\boldsymbol{\Theta}}_e|^{\frac{m_a}{m_b}-1})\big(k_a\boldsymbol{s}_n + k_b\mathrm{sign}(\boldsymbol{s}_n)^{\frac{k_c}{k_d}}\\ &-\boldsymbol{D} + \hat{\boldsymbol{r}}_a(c_1-c_3)\big) - (n_a-1)\boldsymbol{\chi}^T\boldsymbol{\chi} - n_b\boldsymbol{\chi}^T\boldsymbol{\chi}^{\frac{k_c}{k_d}}\\ &-\Psi_1 V_1 - \Psi_2 V_1^{\frac{2l-1}{l}} + \frac{\beta_b m_a}{m_b}|\dot{\boldsymbol{\Theta}}_e|^{\frac{m_a}{m_b}-1}\boldsymbol{s}_n(c_1-c_3)\\ &-\sigma\mu_1\sum_{i=1}^{3}\tilde{r}_{a,i}\hat{r}_{a,i} - \sigma\mu_1\sum_{i=1}^{3}\tilde{r}_{a,i}\hat{r}_{a,i}^{\mu_3} + \Delta_1. \end{aligned} \quad (41)$$

By adding and subtracting a term $\bar{\boldsymbol{r}}_a(c_1-c_3)$ to the right-hand side of (41), then (41) can be turned into

$$\begin{aligned}\dot{V}_3 \leq &-\frac{\beta_b m_a}{m_b}\boldsymbol{s}_n^T\mathrm{diag}(|\dot{\boldsymbol{\Theta}}_e|^{\frac{m_a}{m_b}-1})\big(k_a\boldsymbol{s}_n + k_b\mathrm{sign}(\boldsymbol{s}_n)^{\frac{k_c}{k_d}}\\ &-\boldsymbol{D} + \hat{\boldsymbol{r}}_a(c_1-c_3) + \bar{\boldsymbol{r}}_a(c_1-c_3) - \bar{\boldsymbol{r}}_a(c_1-c_3)\big)\\ &-(n_a-1)\boldsymbol{\chi}^T\boldsymbol{\chi} - n_b\boldsymbol{\chi}^T\boldsymbol{\chi}^{\frac{k_c}{k_d}} - \Psi_1 V_1 - \Psi_2 V_1^{\frac{2l-1}{l}}\\ &+\frac{\beta_b m_a}{m_b}|\dot{\boldsymbol{\Theta}}_e|^{\frac{m_a}{m_b}-1}\boldsymbol{s}_n(c_1-c_3)\tilde{\boldsymbol{r}}_a - \sigma\mu_1\sum_{i=1}^{3}\tilde{r}_{a,i}\hat{r}_{a,i}\\ &-\sigma\mu_2\sum_{i=1}^{3}\tilde{r}_{a,i}\hat{r}_{a,i}^{\mu_3} + \Delta_1\\ =&-\frac{\beta_b m_a}{m_b}\boldsymbol{s}_n^T\mathrm{diag}(|\dot{\boldsymbol{\Theta}}_e|^{\frac{m_a}{m_b}-1})\big(k_a\boldsymbol{s}_n + k_b\mathrm{sign}(\boldsymbol{s}_n)^{\frac{k_c}{k_d}}\\ &+\tilde{\boldsymbol{r}}_a(c_1-c_3)\big) - (n_a-1)\boldsymbol{\chi}^T\boldsymbol{\chi} - n_b\boldsymbol{\chi}^T\boldsymbol{\chi}^{\frac{k_c}{k_d}} - \Psi_1 V_1\\ &-\Psi_2 V_1^{\frac{2l-1}{l}} + \frac{\beta_b m_a}{m_b}|\dot{\boldsymbol{\Theta}}_e|^{\frac{m_a}{m_b}-1}\boldsymbol{s}_n(c_1-c_3)\tilde{\boldsymbol{r}}_a\\ &-\frac{\beta_b m_a}{m_b}\boldsymbol{s}_n^T\mathrm{diag}(|\dot{\boldsymbol{\Theta}}_e|^{\frac{m_a}{m_b}-1})(c_1-c_3)\boldsymbol{r}_0\\ &-\sigma\mu_1\sum_{i=1}^{3}\tilde{r}_{a,i}\hat{r}_{a,i} - \sigma\mu_2\sum_{i=1}^{3}\tilde{r}_{a,i}\hat{r}_{a,i}^{\mu_3} + \Delta_1. \end{aligned} \quad (42)$$

With the help of Lemmas 1 and 5, one can derive

$$-\sigma\mu_1\tilde{r}_{a,i}\hat{r}_{a,i} \leq -\frac{\sigma\mu_1}{2}\tilde{r}_{a,i}^2 + \frac{\sigma\mu_1}{2}\bar{r}_{a,i}^2 \quad (43a)$$

$$-\sigma\mu_2\tilde{r}_{a,i}\hat{r}_{a,i}^{\mu_3} \leq -\frac{\sigma\mu_2(1-\mu_4)}{(1+\mu_3)}\tilde{r}_{a,i}^{1+\mu_3} \quad (43b)$$

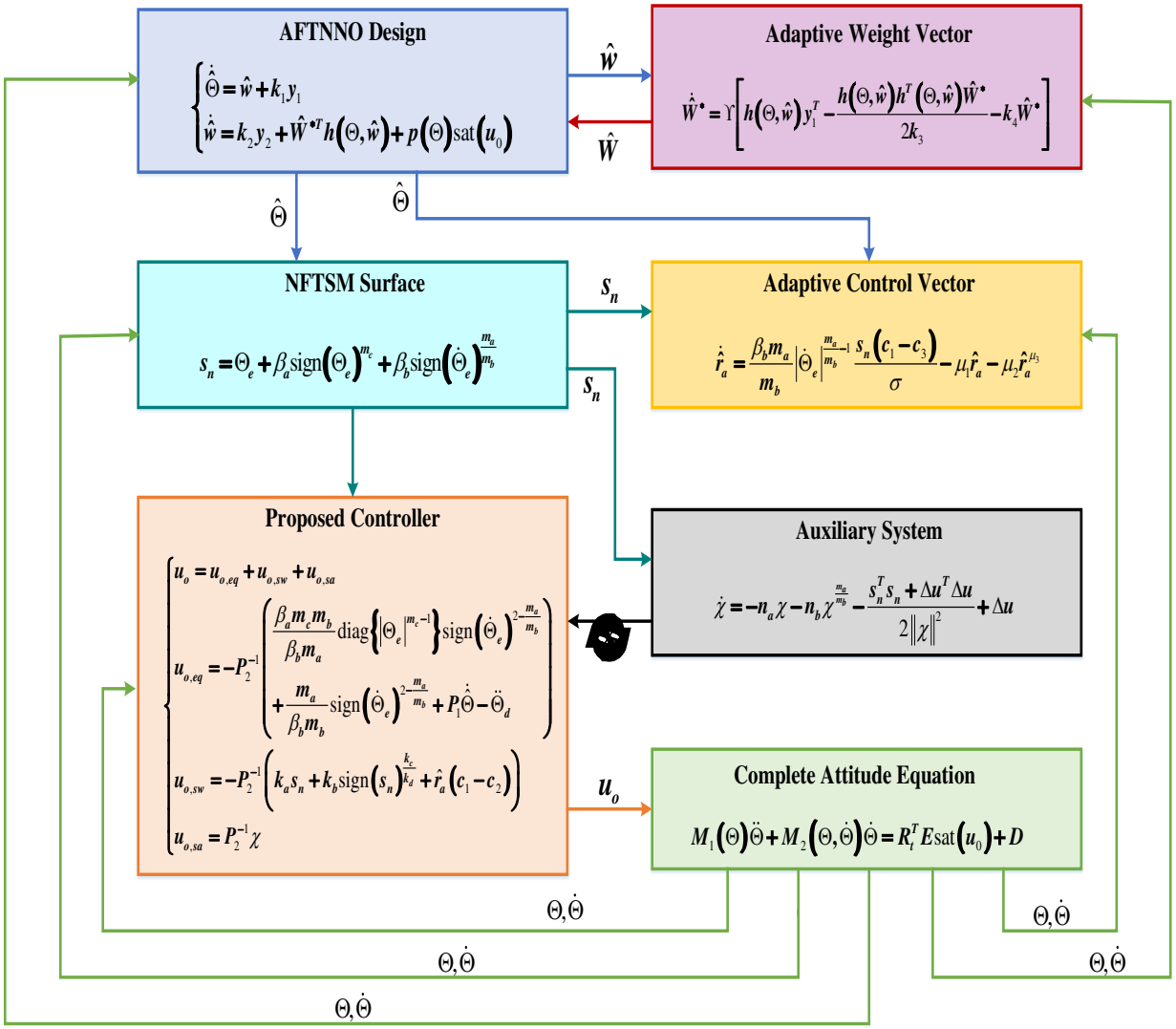

Fig. 5 Block diagram of the proposed control scheme

where $0 < \mu_4 < 1$.

Combing (42) and (43), leads to

$$\begin{aligned}\dot{V}_3 \leq & -\lambda_{\min}(\boldsymbol{L}_1)\boldsymbol{s}_n^T\boldsymbol{s}_n - \lambda_{\min}(\boldsymbol{L}_2)\|\boldsymbol{s}_n\|^{\frac{k_c+k_d}{k_d}} - n_b\|\boldsymbol{\chi}\|^{\frac{k_c+k_d}{k_d}} \\ & - (n_a-1)\boldsymbol{\chi}^T\boldsymbol{\chi} - \Psi_1 V_1 - \Psi_2 V_1^{\frac{2l-1}{l}} - \frac{\sigma\mu_1}{2}\sum_{i=1}^{3}\tilde{r}_{a,i}^2 \\ & - \frac{\sigma\mu_2(1-\mu_4)}{(1+\mu_3)}\sum_{i=1}^{3}\tilde{r}_{a,i}^{1+\mu_3} + \frac{\sigma\mu_1}{2}\sum_{i=1}^{3}\bar{r}_{a,i}^2 + \Delta_1 \\ \leq & -L_5 V_3 - L_6 V_3^{\frac{2l-1}{l}} + \Delta_2 \end{aligned} \tag{44}$$

where $L_5 = \min\{2\lambda_{\min}(\boldsymbol{L}_1), 2(n_a-1), \Psi_1, \mu_1\}$, $L_6 = \min\left\{2^{\frac{k_c+k_d}{2k_d}}\lambda_{\min}(\boldsymbol{L}_2), 2^{\frac{k_c+k_d}{2k_d}}n_b, \Psi_2, \frac{2\mu_2(1-\mu_4)}{(1+\mu_3)}\right\}$, $\mu_3 = 3-\frac{2}{l}$, and $\Delta_2 = \Delta_1 + \frac{\sigma\mu_1}{2}\sum_{i=1}^{3}\bar{r}_{a,i}^2$. Based on Lemma 3, the finite-time stability can be proven and the convergent time T_{reach} is computed by $T_{\text{reach}} \leq T_0 + \max\left\{\frac{l}{\epsilon_0 L_5(1-l)}\ln\frac{\epsilon_0 L_5 V^{\frac{1-l}{l}}(T_0)+L_6}{L_6}, \frac{l}{L_5(1-l)}\ln\frac{L_5 V^{\frac{1-l}{l}}(T_0)+\epsilon_0 L_6}{\epsilon_0 L_6}\right\}$, where $0 < \epsilon_0 < 1$ and T_0 is the initial time. Moreover, it readily follows that the tracking signals of the whole system shall drive into following bounded regions near the origin, as follows:

$$\begin{cases} \|\tilde{\boldsymbol{\Theta}}\| \leq k_3^{-1}\lambda_{\min}^{-\frac{1}{2}}(\boldsymbol{C})\min\left\{\frac{\Delta_2}{(1-\epsilon_2)L_5}, \left(\frac{\Delta_2}{(1-\epsilon_2)L_6}\right)^{\frac{1}{2(1-l)}}\right\} \\ \|\tilde{\boldsymbol{w}}\| \leq \lambda_{\min}^{-\frac{1}{2}}(\boldsymbol{C})\min\left\{\frac{\Delta_2}{(1-\epsilon_2)L_5}, \left(\frac{\Delta_2}{(1-\epsilon_2)L_6}\right)^{\frac{1}{2(1-l)}}\right\} \\ \|\tilde{\boldsymbol{W}}^*\| \leq \lambda_{\min}^{-\frac{1}{2}}(\boldsymbol{\Upsilon}^{-1})\min\left\{\frac{\Delta_2}{(1-\epsilon_2)L_5}, \left(\frac{\Delta_2}{(1-\epsilon_2)L_6}\right)^{\frac{1}{2(1-l)}}\right\} \\ \|\boldsymbol{s}_n\| \leq \sqrt{2}\min\left\{\frac{\Delta_2}{(1-\epsilon_2)L_5}, \left(\frac{\Delta_2}{(1-\epsilon_2)L_6}\right)^{\frac{1}{2(1-l)}}\right\} \\ |\tilde{r}_{a,i}| \leq \frac{\sqrt{2\sigma}}{\sigma}\min\left\{\frac{\Delta_2}{(1-\epsilon_2)L_5}, \left(\frac{\Delta_2}{(1-\epsilon_2)L_6}\right)^{\frac{1}{2(1-l)}}\right\} \end{cases} \tag{45}$$

where $0 < \epsilon_2 < 1$. Next, the finite-time error convergence for $\boldsymbol{\Theta}_e$ is further studied. First, we notice that

(30) can be transformed into the following form

$$\left(\boldsymbol{\Theta}_e - \frac{\boldsymbol{s}_n}{2}\right) + \left(\beta_a - \frac{\boldsymbol{s}_n}{2}\text{sign}(\boldsymbol{\Theta}_e)^{-m_c}\right)\text{sign}(\boldsymbol{\Theta}_e)^{m_c} + \beta_b \text{sign}(\dot{\boldsymbol{\Theta}}_e)^{\frac{m_a}{m_b}} = 0. \quad (46)$$

With attention to Lemma 5 and Remark 5 given in [30], it follows that (46) can be maintained in the form of FNTSM manifold if the following conditions are held:

$$2\boldsymbol{\Theta}_e - \boldsymbol{s}_n > 0,\ 2\beta_a - \boldsymbol{s}_n \text{sign}(\boldsymbol{\Theta}_e)^{-m_c} > 0. \quad (47)$$

From (47), it can be concluded that the tracking error $\boldsymbol{\Theta}_e$ will eventually converge into the bounded region, as

$$\|\boldsymbol{\Theta}_e\| \leq \max\left\{\frac{\Xi}{2}, \left(\frac{\Xi}{2\beta_a}\right)^{\frac{1}{m_c}}\right\} \quad (48)$$

where $\Xi = \sqrt{2}\min\left\{\left(\frac{\Delta_2}{(1-\epsilon_2)L_6}\right)^{\frac{1}{2(1-l)}}, \frac{\Delta_2}{(1-\epsilon_2)L_5}\right\}$. Further, the total convergence time T_{total} is given by

$$T_{\text{total}} = T_{\text{reach}} + T_{\text{sliding}} \quad (49)$$

where T_{reach} represents the time that it spends to arrive at the convergence region of NFTSM manifold $\boldsymbol{s}_n$ and it has been directly given earlier, and meanwhile, T_{sliding} represents the time that it spends to arrive at the convergence region of tracking error $\boldsymbol{\Theta}_e$ and which can be calculated according to Remark 5 given in [30], that is, $T_{\text{sliding}} = \frac{m_a\|\boldsymbol{\Theta}_e(0)\|^{1-\frac{m_b}{m_a}}}{\beta_b(m_a-m_b)} \cdot \Lambda\left(\frac{m_b}{m_a}, \frac{m_a-m_b}{(m_c-1)m_a}, 1 + \frac{m_a-m_b}{(m_c-1)m_a}, -\beta_a\|\boldsymbol{\Theta}_e(0)\|^{m_c-1}\right)$. Due to the facts that $(1+\frac{m_a-m_b}{(m_c-1)m_a}) - \frac{m_a-m_b}{(m_c-1)m_a} - \frac{m_b}{m_a} = 1 - \frac{m_b}{m_a} \in (0, \frac{1}{2})$ and $-\beta_a\|\boldsymbol{\Theta}_e(0)\|^{m_c-1} < 0$, it follows that by means of Lemma 4, the function $\Lambda(\cdot)$ will keep convergent. Therefore, the proof of Theorem 2 is completed.

3.3 Control Parameters Selection

Since the attitude tracking performance is usually compromised with actuator faults, constrained inputs, and especially, with various uncertainties and disturbances, some control parameters should be thoroughly selected. In this study, the error convergence regions (49) can be adjusted to arbitrary small neighbourhoods by selecting tunable parameters suitably. As a result, the relevant selection criteria of controller parameters are clearly stated, as follows:

1) *Selections of parameters* $m_i,\ (i = a, b, c)$*:* To improve the convergence rate, the lager values $\frac{m_a}{m_b}$ and m_c are often chosen under the premise of satisfying the conditions $1 < \frac{m_a}{m_b} < 2$ and $m_c > \frac{m_a}{m_b}$. The other way round, this may cause more serious chattering. Thus, we should make an acceptable trade-off between the convergence speed and the control chattering. Luckily, a fast-type reaching control law is designed in this study, which is conducive to the chattering suppression and the improvement of convergence speed.
2) *Selections of parameters* $\beta_i, n_i,\ (i = a, b)$*:* The increase of parameters β_a and β_b can achieve a shorter setting time and the smaller error convergence regions. However, overlarge β_a may lead to a larger control input in (39). Under the condition that the parameter n_a must satisfy $n_a > 1$, a large value n_a can quickly eliminate the saturation error, while it is easy to cause overcompensation if the value n_a is too big. For the parameter n_b, it only plays a role in achieving a finite-time convergence.
3) *Selections of parameters* σ *and* $\mu_i,\ (i = 1, 2, 3)$*:* The parameter σ determines the update rate for adaptive variable $\hat{\boldsymbol{r}}_a$, which can be allowed to choose small enough in order to improve the update rate. In turn, this leads to overestimation and input saturation. In practice, the parameter σ should be adjusted based on a trial and error manner. Furthermore, the appropriate choice of parameter μ_i can ensure the finite-time convergence property and avoid the drift of variable $\hat{\boldsymbol{r}}_a$.
4) *Selections of parameters* $k_i,\ (i = a, b, c, d)$*:* In many references [32, 33, 37], the bigger gains k_a and k_b should be selected to overcome the big lumped disturbance. It should be noted that the overlarge gains are prone to input saturation and energy waste, while too small gains fail to attain a fast finite-time convergence. Fortunately, we design an adaptive FLS to compensate for the lumped disturbance, and hence the smaller values k_a and k_b can be selected. Moreover, because the term $\text{sign}(\boldsymbol{s}_n)^{\frac{k_c}{k_d}}$ with $\frac{k_c}{k_d} \in (0, 1)$ is designed to enhance the system robustness, and displays like a bridge between the linear control if $\frac{k_c}{k_d} \to 1$ and the discontinuous control if $\frac{k_c}{k_d} \to 0$ [24], a bigger value $\frac{k_c}{k_d}$ tends to reduce the signal chattering but at the price of lower robustness. Therefore, we should conduct a satisfactory balance between chattering elimination and strong robustness for the selection of $\frac{k_c}{k_d}$.

4 Numerical Simulations

4.1 Parameter Setting

The numerical simulations are performed in the MATLAB/Simulink software environment by employing a

Table 2 Physical parameters of the quadrotor UAV

Variable	Description	Value (Unit)
m	Total mass of the quadortor UAV	2 (kg)
l_d	Distance from the rotor to the centroid	0.2 (m)
$\underline{u}_i$, $\overline{u}_i$	Lower and upper bounds of $u_{o,i}$	35 (N)
$J_{0,x}$, $J_{0,y}$, $J_{0,z}$	Inertial coefficients	0.01175, 0.01175, 0.02229 ($\mathrm{N \cdot m \cdot s^2/rad}$)
κ_a	Lift coefficient	2
κ_b	Drag factor	5

Table 3 Simulation parameters of compared controllers

Controllers	Design simulation parameters
PD	$P = 0.6$, $D = 0.2$.
DSC	$k_m = k_n = 0.23$, $\tau_s = 0.01$.
AFTC	$v_a = 1.2$, $v_b = -1.2$, $\sigma = 0.05$, $\mu_1 = \mu_2 = 0.015$, $\mu_3 = 0.002$, $\hat{\boldsymbol{r}}_a = [0;0;0]$ $m_a = 19$, $m_b = 17$, $m_c = 1.1$, $k_a = k_b = 40$, $k_c = 13$, $k_d = 15$, $\beta_a = 3$, $\beta_b = 0.1$, $l = \frac{8}{9}$, $k_1 = 0.0001$, $k_2 = 0.0005$, $k_3 = 0.2$, $k_4 = 0.1$, $\kappa = 2$, $\boldsymbol{\Upsilon} = \mathrm{diag}\{10,10,10\}$, $\hat{\boldsymbol{\Theta}}(0) = [0;0;0]$, $\hat{\boldsymbol{w}}(0) = [0;0;0]$, $\hat{\boldsymbol{W}}^*(0) = [0;0;0]$.
Proposed method	$v_a = 1.2$, $v_b = -1.2$, $\sigma = 0.05$, $\mu_1 = \mu_2 = 0.015$, $\mu_3 = 0.002$, $\hat{\boldsymbol{r}}_a = [0;0;0]$ $m_a = 19$, $m_b = 17$, $m_c = 1.1$, $k_a = k_b = 40$, $k_c = 13$, $k_d = 15$, $\beta_a = 3$, $\beta_b = 0.1$, $l = \frac{8}{9}$, $k_1 = 0.0001$, $k_2 = 0.0005$, $k_3 = 0.2$, $k_4 = 0.1$, $\kappa = 2$, $\boldsymbol{\Upsilon} = \mathrm{diag}\{10,10,10\}$, $\hat{\boldsymbol{\Theta}}(0) = [0;0;0]$, $\hat{\boldsymbol{w}}(0) = [0;0;0]$, $\hat{\boldsymbol{W}}^*(0) = [0;0;0]$, $n_a = 15$, $n_b = 10$, $\boldsymbol{\chi} = [0;0;0]$.

Abbreviation: Proportion-differentiation (PD), Dynamic surface control (DSC), Adaptive fault-tolerant control (AFTC).

Notation: (i) The mathematical form of PD control is expressed in this study as $u_{PD} = P\boldsymbol{\Theta}_e + D\dot{\boldsymbol{\Theta}}_e$; (ii) Based on the work of [5], the expression of DSC strategy is given as follows: $u_{DSC} = [\boldsymbol{R}_s^T]^{-1}(\boldsymbol{M}_1(\boldsymbol{\Theta})\dot{\boldsymbol{v}}_k - \boldsymbol{\Theta}_e - k_n\boldsymbol{e}_1)$, where $\boldsymbol{e}_1 = \dot{\hat{\boldsymbol{\Theta}}} - \boldsymbol{v}_k$, $\boldsymbol{v}_k + \tau_s\dot{\boldsymbol{v}}_k = \bar{\boldsymbol{v}}_k$, and $\bar{\boldsymbol{v}}_k = -k_m\boldsymbol{\Theta}_e + \dot{\boldsymbol{\Theta}}_d$; (iii) Compared with the AFTC scheme, the proposed method with an additional auxiliary system has the ability to deal with the problem of input saturation.

fixed-step Runge-Kutta solver and are compared with PD, DSC, and AFTC methods, where the sampling frequency is set as 100 Hz. The physical parameters of the quadrotor UAV used in this study are specifically given in Table 2.

In the simulation, the desired attitude trajectory is chosen as $\boldsymbol{\Theta}_d(t) = [\phi_d(t), \theta_d(t), \varphi_d(t)]^T = [0.6\cos(0.5t)(1-\cos(0.7t)), 0.6\sin(0.7t)(1-\cos(0.45t)), 0.8\sin(0.1t)\sin(0.4t)]^T$, and the initial states of the real attitude trajectory in the above-mentioned four controllers are randomly selected such that $\boldsymbol{\Theta}(0) = [\phi(0), \theta(0), \varphi(0)]^T = [1, -1, 1]^T$. The signals of external disturbances, uncertain inertia matrix, and actuator faults are presented in Fig. 6. Furthermore, the sensor noise is added in order to better simulate the actual flight condition, which is set as a 0.1 level. Here should be noticed that the simulation parameters of compared controllers are completely shown in Table 3.

4.2 Result Analysis

The control results of the comparative simulation are depicted from Fig. 7 to Fig. 13. As can be seen from Fig. 7, it is obvious that the PD approach has a larger oscillations than the other remaining controllers in terms of attitude angles, which illustrates that the PD controller is susceptible to uncertain parameters, external disturbances, and actuator faults. To be precise, the tracking errors under various controllers are plotted in Fig. 8. From Fig. 8, it is clear that the tracking errors of the AFTC and proposed methods are smaller than that of the PD and DSC methods. The control input commands are presented in Fig. 9, which reflects that the proposed controller was capable of achieving the chattering elimination and saturation suppression. Fig. 10 shows that the sliding surfaces are smooth and quickly reach near zero. The evolution of the adaptive gain in the proposed controller is provided in Fig. 11, and the problem of parameter drifting be avoided effectively. From Fig. 12, the designed AFTNNO can realize the estimation for the attitude angular velocity even under these adverse effects. In addition, the adaptive weight parameter is presented in Fig. 13, in which the parameters can accomplish a rapid convergence performance.

To quantitatively analyze the tracking performance of various controllers, four performance indices are employed in this study and are concretely described in the following forms:

1) Average squared error (ASE):

$$\mu_{ASE} = \frac{1}{N}\sum_{i=1}^{N}\left(\phi_e^2(i) + \theta_e^2(i) + \psi_e^2(i)\right). \tag{50}$$

Since the ASE index penalizes a bigger error more than a smaller one, one can illustrate that the designed control algorithm provides a fast convergent speed if the ASE value is lower.

2) Average absolute error (AAE):

$$\mu_{AAE} = \frac{1}{N}\sum_{i=1}^{N}\left(|\phi_e(i)| + |\theta_e(i)| + |\psi_e(i)|\right). \tag{51}$$

In contrast to the ASE index, the AAE index possesses a slower convergent rate but with less persistent oscillation.

3) Average time-weighted absolute error (ATAE):

$$\mu_{ATAE} = \frac{1}{N}\sum_{i=1}^{N}\left(i|\phi_e|(i) + i|\theta_e(i)| + i|\psi_e(i)|\right). \tag{52}$$

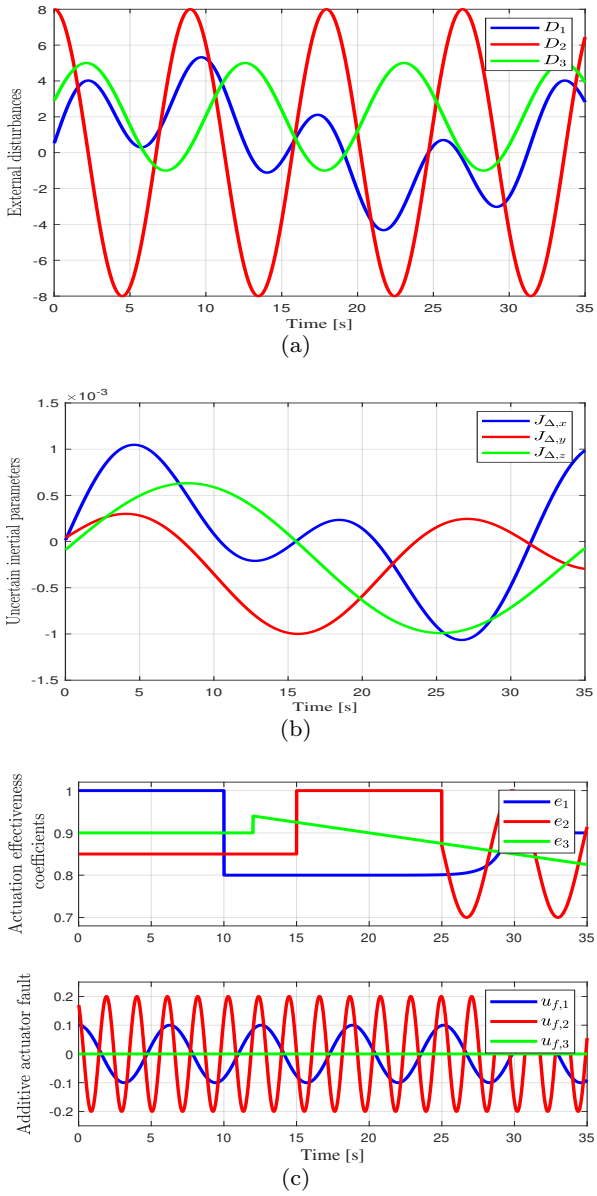

Fig. 6 Time response of the attitude angle.

The ATAE index pays close attention to steady-state error, but it thinks little of the initial errors. This problem can be overcome based on the simultaneous consideration of ASE and AAE indices.

4) Total energy consumption (TEC):

$$\mu_{TEC} = \frac{1}{N}\sum_{i=1}^{N}\left(|u_1(i)| + |u_2(i)| + |u_3(i)| + |u_4(i)|\right) \tag{53}$$

The smaller TEC value reflects the developed control scheme can reduce the energy consumption.

where N denotes the total time of the simulation operation. Therefore, these performance indices are applied to fairly evaluate the tracking performance of the different controllers. Moreover, it should be especially emphasized that these indices are expected to be as small as possible.

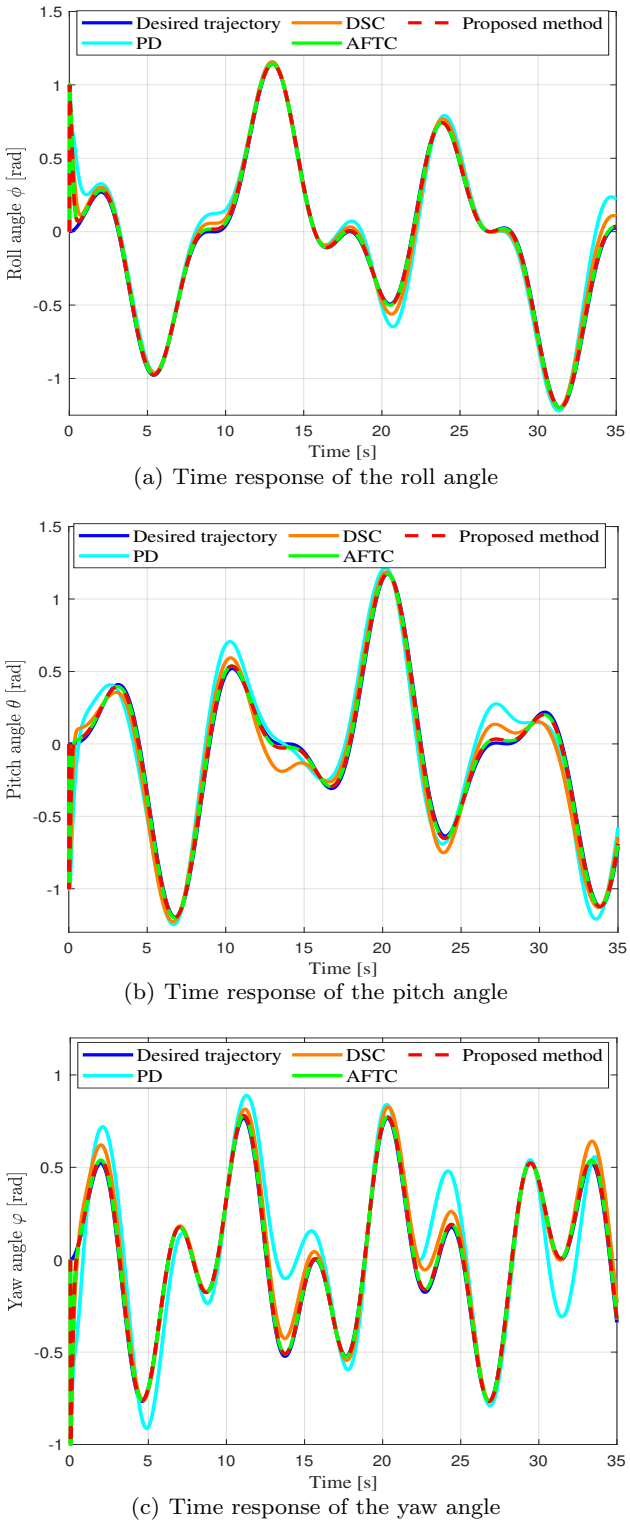

Fig. 7 Time response of the attitude angle.

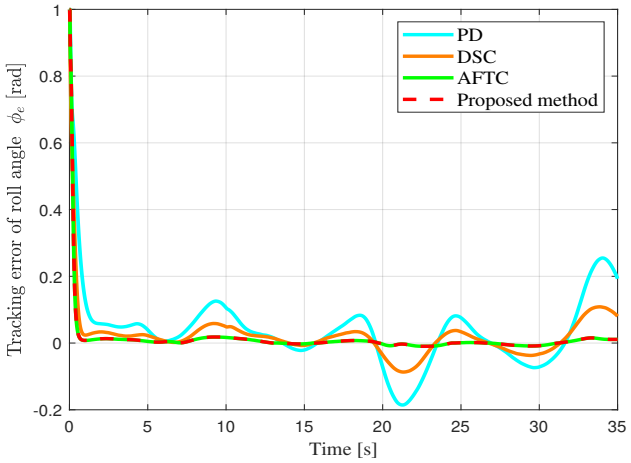

(a) Time response of the roll angle error

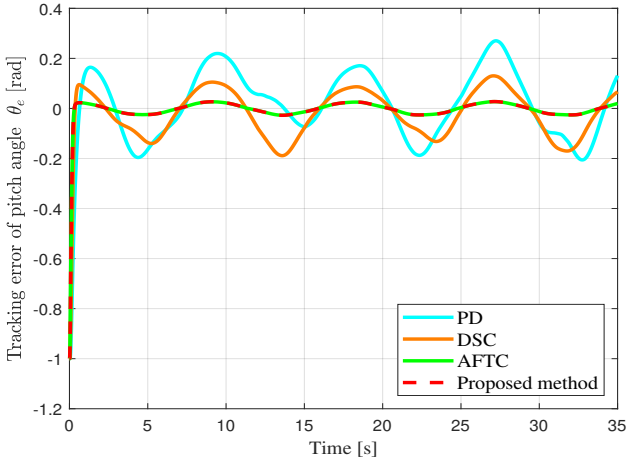

(b) Time response of the pitch angle error

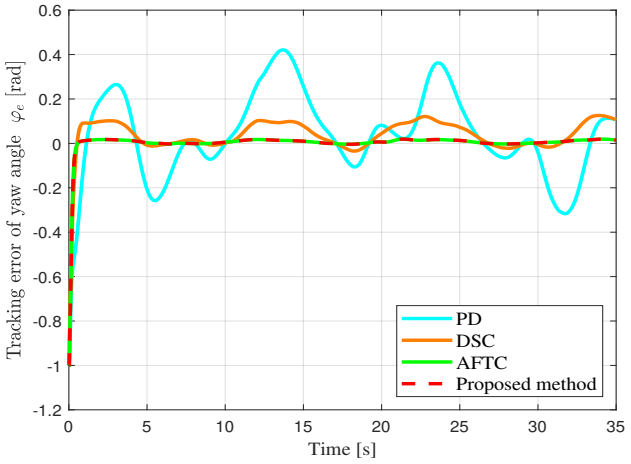

(c) Time response of the yaw angle error

Fig. 8 Time response of the attitude angle error.

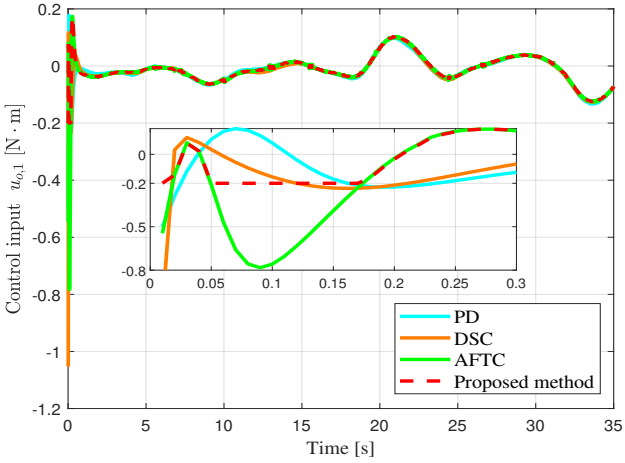

(a) Time response of the control input in the roll channel

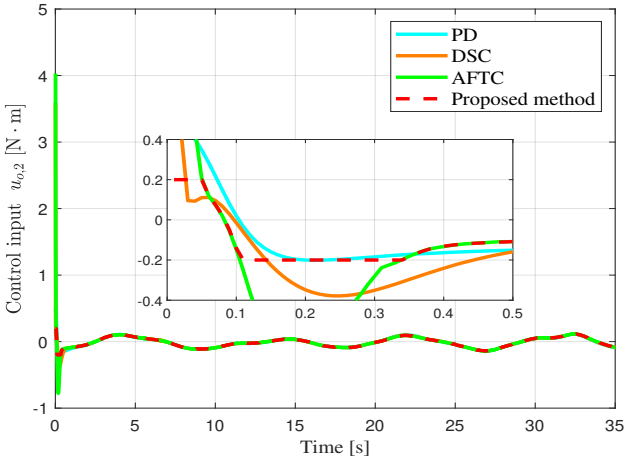

(b) Time response of the control input in the pitch channel

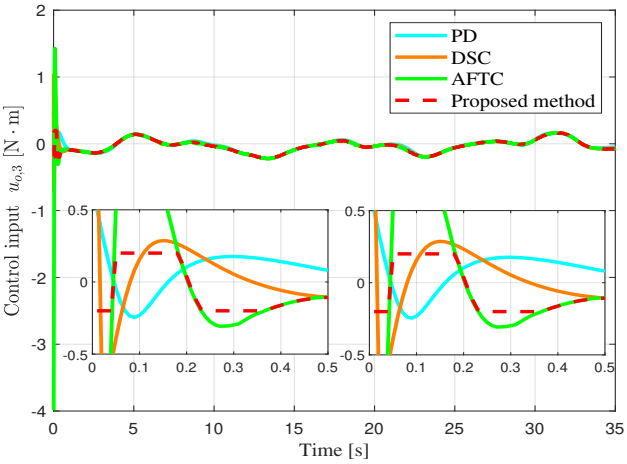

(c) Time response of the control input in the yaw channel

Fig. 9 Time response of the control input.

The statistical conclusions in terms of aforesaid performance indices are visually presented in Fig. 14 to better observe the superiority of the designed control scheme. By analyzing Fig. 13, we can obtain the following results: (i) The values of all performance indices for PD control are the largest, which reflects that PD control provides a worse robustness; (ii) Although the performance of DSC strategy is better than that of PD con-

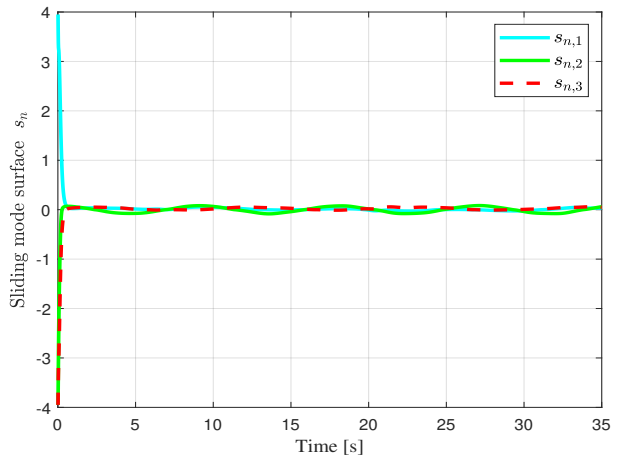

Fig. 10 Time response of sliding mode surface under the proposed controller.

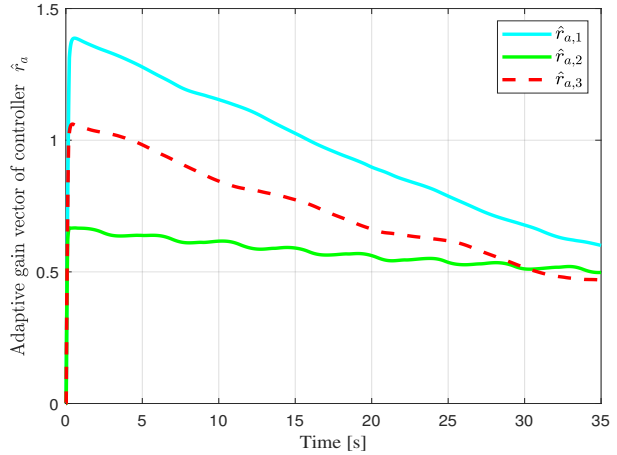

Fig. 11 Time response of adaptive gain vector under the proposed controller.

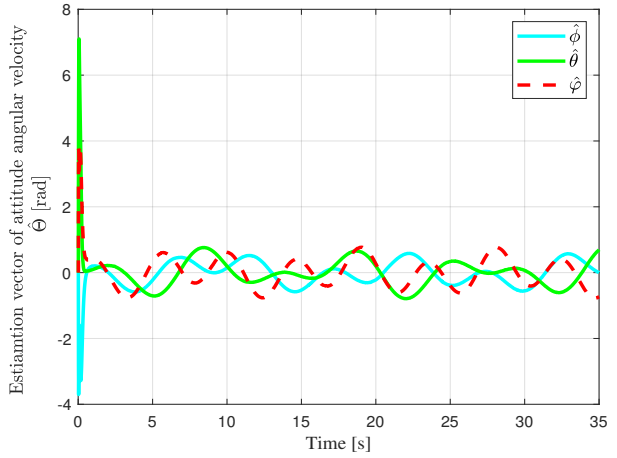

Fig. 12 Time response of the estimation for the attitude angular velocity.

trol, there is much room for improvement in ISE, IAE, and ITAE indices compared with the AFTC method; (iii) In contrast to the AFTC method, the proposed

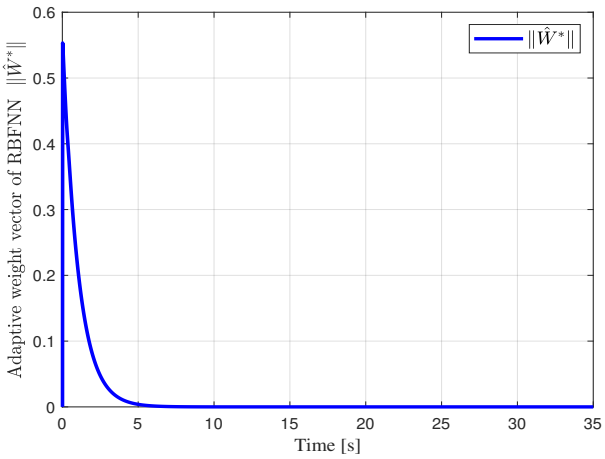

Fig. 13 Time response of adaptive weight in the RBFNN.

controller successfully overcomes the input saturation without the cost of robustness degradation, for this point, the proposed controller is almost the same in ISE, IAE, and ITAE indices, but has a great enhancement in the TEC index. Consequently, the above analyses illustrate that despite the existence of parametric uncertainty, external disturbance, actuator fault, and input saturation, the proposed controller can still achieve high-performance attitude tracking of quadrotor UAV in aspects of strong robustness, chattering elimination, saturation alleviation, and fault-tolerant.

5 Conclusions and Future Works

In this study, a robust intelligent fault-tolerant based finite-time attitude tracking control strategy for quadrotor UAVs subject to the parametric uncertainty, external disturbance, input saturation, and actuator faults, which is not only of research value but also academically challenging. Firstly, an AFTNNO is developed to measure the information of angular velocity after a finite time. To deal with the problem of parametric uncertainty, external disturbance, and actuator faults, a novel switching control law including the adaptive FLS and the continuous controller is constructed, which can avoid the choice of big gains and does not the prior information of the lumped disturbance bounds. In addition, to attenuate the effect of actuator constraint, an auxiliary system is further developed. Comprehensive comparisons show that the designed control framework shows remarkably superior performance. Recognizing these advantages, in further research, we are ready to perform the real-time experiments to better verify the practical feasibility of the proposed control strategy.

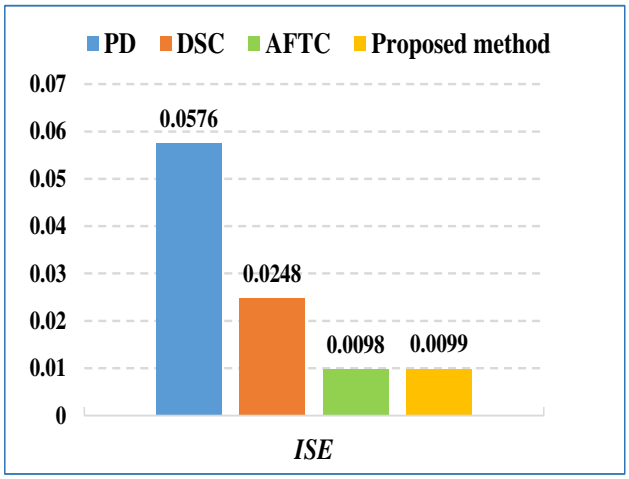

(a) The value of ISE index

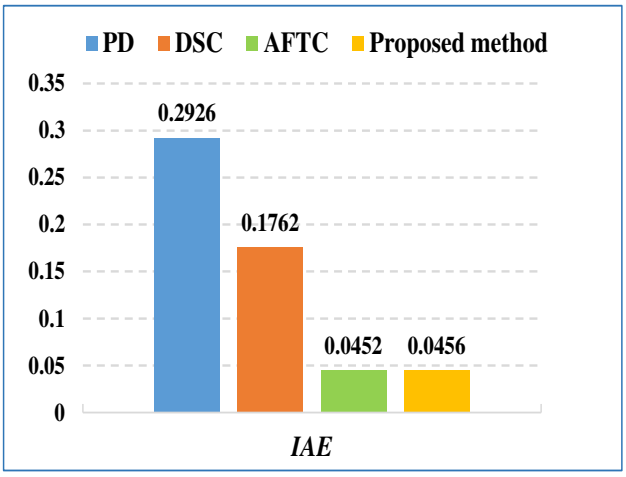

(b) The value of IAE index

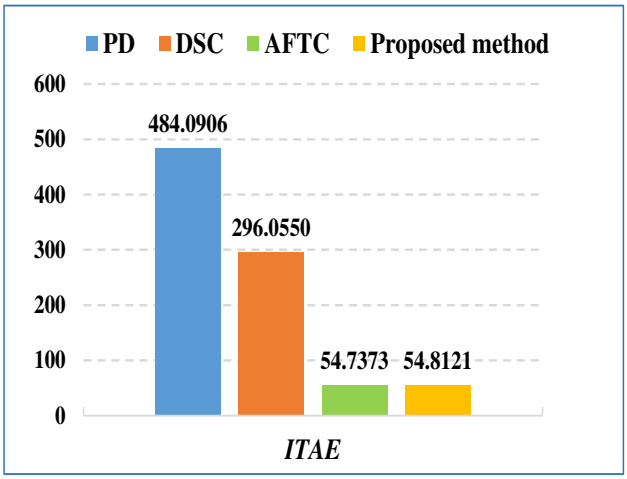

(c) The value of ITAE index

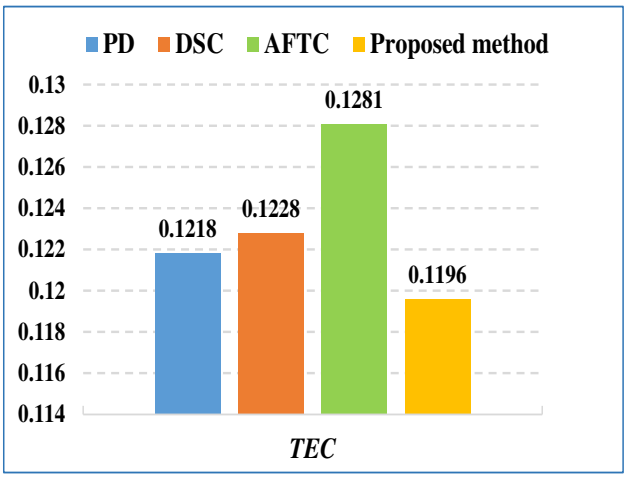

(d) The value of TEC index

Fig. 14 Comparison of performance index values.

Acknowledgements This work was supported by the National Natural Science Foundation of China (No. 31671586).

Conflict of interest statement The authors declare that they have no conflict of interest.

Data availability statements Data sharing not applicable to this article as no datasets were generated or analysed during the current study

References

1. B. Xian, S. Wang, and S. Yang, "Nonlinear adaptive control for an unmanned aerial payload transportation system: theory and experimental validation," *Nonlinear Dyn.*, vol. 98, pp. 1745–1760, Oct. 2019.
2. Y. Zou and Z. Meng, "Immersion and invariance-based adaptive controller for quadrotor systems," *IEEE Trans. Syst., Man, Cybern., Syst.*, vol. 49, no. 11, pp. 2288–2297, Nov. 2019.
3. C. Mi and Y. Zhang, "Learning-based robust tracking control of quadrotor with time-varying and coupling uncertainties," *IEEE Trans. Neural Netw. Learn. Syst.*, vol. 31, no. 1, pp. 259–273, Jan. 2020.
4. U. Ansari, A. H. Bajodah, and B. Kada, "Development and experimental investigation of a qadrotor's robust generalized dynamic inversion control system," *Nonlinear Dyn.*, vol. 96, pp. 1541–1557, Mar. 2019.
5. K. Liu and R. Wang, "Antisaturation command filtered backstepping control based disturbance rejection for a quadarotor UAV," *IEEE Trans. Circuits Syst. II: Express Briefs*, to be published, DOI: 10.1109/TCSII.2021.3069967.
6. Z. Zhu, Y. Xia, and M. Fu, "Observer-based output feedback attitude stabilization for spacecraft with finite-time convergence," *IEEE Trans. Control Syst. Technol.*, vol. 27, no. 2, pp. 781–789 Mar. 2019.
7. Z. Zhao, D. Cao, J. Yang, and H. Wang, "High-order sliding mode observer-based trajectory tracking control for a quadrotor UAV with uncertain dynamics," *Nonlinear Dyn.*, vol. 102, pp. 2583–2596, Nov. 2020.
8. X. Li, H. Zhang, W. Fan, J. Zhao, and C. Wang, "Multivariable finite-time composite control strategy based on immersion and invariance for quadrotor under mismatched

disturbances," *Aerosp. Sci. Technol.*, vol. 99, pp. 105763, Apir. 2020.
9. Y. Li and Q. Xu, "Adaptive sliding mode control with perturbation estimation and PID sliding surface for motion tracking of a piezo-driven micromanipulator," *IEEE Trans. Control Syst. Technol.*, vol. 18, no. 4, pp. 798–810, Jul. 2010.
10. L. Zhang, L. Liu, Z. Wang, and Y. Xia, "Continuous finite-time control for uncertain robot manipulators with integral sliding mode," *IET Contr. Theory Appl.*, vol. 12, no. 11, pp. 1621–1627, Jul. 2018.
11. Q. Mao, L. Dou, Z. Yang, B. Tian, and Q. Zong, "Fuzzy disturbance observer-based adaptive sliding mode control for reusable launch vehicles with aeroservoelastic characteristic," *IEEE Trans. Ind. Inform.*, vol. 16, no. 2, pp. 1214–1223, Feb. 2020.
12. H. Han, X. Wu, and J. Qiao, "Design of robust sliding mode control with adaptive reaching law," *IEEE Trans. Syst., Man, Cybern., Syst.*, vol. 50, no. 11, pp. 4415–4414, Nov. 2020.
13. K. Liu, X. Wang, R. Wang, G. Sun, and X. Wang, "Antisaturation finite-time attitude tracking control based observer for a quadrotor," *IEEE Trans. Circuits Syst. II: Express Briefs*, to be published, DOI: 10.1109/TCSII.2020.3045769.
14. V. Utkin, "Discussion aspects of high-order sliding mode control," *IEEE Trans. Autom. Control*, vol. 61, no. 3, Mar. 2016.
15. S. Shi, S. Xu, J. Gu, and H. Min, "Global high-order sliding mode controller design subject to mismatched terms: Application to buck converter," *IEEE Trans. Circuits Syst. I, Reg. Papers*, vol. 66, no. 12, Dec. 2019.
16. X. Shao and Y. Shi, "Neural adaptive control for MEMS gyroscope with full-state constraints and quantized input," *IEEE Trans. Ind. Informat*, vol. 16, no. 10, pp. 6444-6454, Oct. 2020
17. X. Zhang, Y. Wang, G. Zhu, X. Chen, Z. Li, C. Wang, and C. -Y. Su, "Compound adaptive fuzzy quantized control for quadrotor and its experimental verification," *IEEE Trans. Cybern.*, to be published, DOI: 10.1109/TCYB.2020.2987811.
18. J. Zhang, Z. Ren, C. Deng, B. Wen, "Adaptive fuzzy global sliding mode control for trajectory tracking of quadrotor UAVs," *Nonlinear Dyn.,* vol. 97, pp. 609–627, Jul. 2019.
19. M. Van and S. S. Ge, "Adaptive fuzzy integral sliding mode control for robust fault tolerant control of robot manipulators with disturbance observer," *IEEE Trans. Fuzzy Syst*, to be published, DOI: 10.1109/TFUZZ.2020.2973955.
20. V. K. Tripathi, A. K. Kamath, L. Behera, N. K. Verma, and S. Nahavandi, "Finite-time super twisting sliding mode controller based on higher-order sliding mode observer for real-time trajectory tracking of a quadrotor," *IET Contr. Theory Appl.*, vol. 14, no. 16, pp. 2359–2371, Nov. 2020.
21. J. Zhou, Y. Cheng, H. Du, D. Wu, M. Zhu, and X. Lin, "Active finite-time disturbance rejection control for attitude tracking of quad-rotor under input saturation," *J. Franklin Inst.*, vol. 357, pp. 11153–11170, Nov. 2020.
22. F. Wang, H. Gao, K. Wang, C. Zhou, Q. Zong, and C. Hua, "Disturbance observer based-finite time control design for a quadrotor UAV with external disturbance," *IEEE Trans. Aerosp. Electron. Syst.*, to be published, DOI: 10.1109/TAES.2020.3046087.
23. S. Kamal, J. A. Moreno, A. Chalanga, B. Bandyopadhyay, and L. M. Fridman, "Continuous terminal sliding-mode controller," *Automatica*, vol. 69, pp. 308–314, Jul. 2016.
24. S. Yu, X. Yu, B. Shirinzadeh, and Z. Man, "Continuous finite-time control for robotic manipulators with terminal sliding mode," *Automatica*, vol. 41, no. 11, pp. 1957–1964, Nov. 2005.
25. K. Eliker and W. Zhang, "Finite-time adaptive integral backstepping fast terminal sliding mode control application on quadrotor UAV," *Int. J. Control Autom. Syst.*, vol. 18, no. 2, pp. 415–430, Feb. 2020.
26. L. A. Tuan, "Neural observer and adaptive fractional-order backstepping fast-terminal sliding-mode control of RTG cranes," *IEEE Trans. Ind. Electron.*, vol. 68, no. 1, pp. 434–442, Jan. 2021.
27. B. Li, H. Ban, W. Gong, and B. Xiao, "Extended state observer-based finite-time dynamic surface control for trajectory tracking of a quadrotor unmanned aerial vehicle," *Trans. Inst. Meas. Control*, vol. 42, no. 15, pp. 2956–2968, Nov. 2020.
28. P. Tang, D. Lin, D. Zheng, S. Fan, and J. Ye, "Observer based finite-time fault tolerant quadrotor attitude control with actuator faults", *Aerosp. Sci. Technol.*, vol. 104, pp. 105968, Sept. 2020.
29. H. Rabiee, M. Ataei, and M. Ekramian, "Continuous nonsingular terminal sliding mode control based on adaptive sliding mode disturbance observer for uncertain nonlinear systems," *Automatica*, vol. 109, pp. 108515, Nov. 2019.
30. L. Yang and J. Yang, "Nonsingular fast terminal sliding-mode control for nonlinear dynamical systems," *Int. J. Robust Nonlin. Control*, vol. 21, no. 16, pp. 1865–1879, Nov. 2011.
31. A. L. Silva and D. A. Santos, "Fast nonsingular terminal sliding mode flight control for multirotor aerial vehicles," *IEEE Trans. Aerosp. Electron. Syst.,* vol. 56, no. 6, pp. 4288–4299, Dec. 2020.
32. J. Li, H. Du, Y. Cheng, G. Wen, X. Chen, and C. Jiang, "Position tracking control for permanent magnet linear motor via fast nonsingular terminal sliding mode control," *Nonlinear Dyn.,* vol. 97, pp. 2595–2605, Sept. 2019.
33. M. Van, S. S. Ge, and H. Ren, "Finite time fault tolerant control for robot manipulators using time delay estimation and continuous nonsingular fast terminal sliding mode control," *IEEE Trans. Cybern.*, vol. 47, no. 7, pp. 1681–1693, Jul. 2017.
34. V. -T. Nguyen, C. -Y. Lin, S. -F. Su, W. Sun, and M. J. Er, "Global finite time active disturbance rejection control for parallel manipulators with unknown bounded uncertainties," *IEEE Trans. Syst., Man, Cybern., Syst.*, to be published, DOI: 10.1109/TSMC.2020.2987056.
35. Z. Zhao, D. Cao, J. Yang, and H. Wang, "High-order sliding mode observer-based trajectory tracking control for a quadrotor UAV with uncertain dynamics," *Nonlinear Dyn.,* vol. 102, pp. 2583–2596, Dec. 2020.
36. J. Fei and C. Lu, "Adaptive fractional order sliding mode controller with neural estimator," *J. Frankl. Inst.*, vol. 355, pp. 2369–2391, Mar. 2018.
37. R. Ji, J. Ma, and S. S. Ge, "Modeling and control of a tilting quadcopter," *IEEE Trans. Aerosp. Electron. Syst.*, vol. 56, no. 4 pp. 2823–2834, Aug. 2020.
38. X. Shao, Q. Meng, J. Liu, and H. Wang, "RISE and disturbance compensation based trajectory tracking control for a quadrotor UAV without velocity measurements," *Aerosp. Sci. Technol.*, vol. 74, pp. 145–159, May 2018.
39. Y. Sun, C. Zheng, and P. Mercorelli, "Velocity-free friction compensation for motion systems with actuator constraint," *Mech. Syst. Signal Proc.*, vol. 148, pp. 107132, Feb. 2021.

40. A. M. Zou, A. H. J. de Ruiter, and K. D. Kumar, "Distributed finite-time velocity-free attitude coordination control for spacecraft formations," *Automatica*, vol. 67, pp. 46–53, May 2016.
41. N. Sun, T. Yang, and Y. Fang, "Transportation control of doublependulum cranes with a nonlinear quasi-PID scheme: Design and experiments," *IEEE Trans. Syst. Man Cybern. Syst.*, vol. 49, no. 7, pp. 1408–1418, Jul. 2019.
42. Z. Yu, Y. Zhang, B. Jiang, C. -Y. Su, J. Fu, Y. Jin, and T. Chai, "Nussbaum-based finite-time fractional-order backstepping fault-tolerant flight control of fixed-wing UAV against input saturation with hardware-in-the-loop validation," *Mech. Syst. Signal Proc.*, vol. 153, pp. 107406, May 2021.
43. M. Chen, B. Ren, Q. Wu, and C. Jiang, "Anti-disturbance control of hypersonic flight vehicles with input saturation using disturbance observer," *Sci. China Inf. Sci.*, vol. 58, pp. 1–12, Jul. 2015.
44. K. Liu, H. Ji, and Y. Zhang, "Extended state observer based adaptive sliding mode tracking control of wheeled mobile robot with input saturation and uncertainties," *Proc. Inst. Mech. Eng. Part C-J. Eng. Mech. Eng. Sci.*, vol. 233, no. 15, pp. 5460–5476, Aug. 2019.
45. H. Yi and Y. Jia, "Adaptive finite-time 6-DOF tracking control for spacecraft fly around with input saturation and state constraints," *IEEE Trans. Aerosp. Electron. Syst.*, vol. 55, no. 6, pp. 3259-3272, Dec. 2019.
46. S. Harshavarthini, R. Sakthivel, and C. K. Ahn, "Finite-time reliable attitude tracking control design for nonlinear quadrotor model with actuator faults," *Nonlinear Dyn.,* vol. 96, pp. 2681–2692, Apr. 2020.
47. S. Zeghlache, A. Djerioui, L. Benyettou, T. Benslimane, H. Mekki, and A. Bouguerra, "Fault tolerant control for modified quadrotor via adaptive type-2 fuzzy backstepping subject to actuator faults," *ISA Trans.,* vol. 95, pp. 330–345, Dec. 2019.
48. X. Nian, W. Chen, X. Chu, and Z. Xu, "Robust adaptive fault estimation and fault tolerant control for quadrotor attitude systems," *Int. J. Control*, vol. 93, no. 3, pp. 725–737, Mar. 2020.
49. Q. Hu and B. Jiang, "Continuous finite-time attitude control for rigid spacecraft based on angular velocity observer," *IEEE Trans. Aerosp. Electron. Syst.*, vol. 54, no. 3, pp. 1082–1092, Jun. 2018.
50. S. -K. Kim and C. K. Ahn, "Angular velocity observer-based quadcopter attitude stabilization via pole-zero cancellation technique," *IEEE Trans. Circuits Syst. II: Express Briefs*, to be published, DOI: 10.1109/TCSII.2021.3055903.
51. A. M. Zou and Z. Fan, "Fixed-time attitude tracking control for rigid spacecraft without angular velocity measurements," *IEEE Trans. Ind. Electron.*, vol. 67, no. 8, pp. 6795–6805, Aug. 2020.
52. J. Cao, H. X. Li, and D. W. C. Ho, "Synchronization criteria of lur'e systems with time-delay feedback control," *Chaos, Solitons Fractals*, vol. 23, no. 4, pp. 1285–1298, Feb. 2005.
53. J. Yu, P. Shi, and L. Zhao, "Finite-time command filtered backstepping control for a class of nonlinear systems," *Automatica,* vol. 92, pp. 173–180, Jun. 2018.

Figures

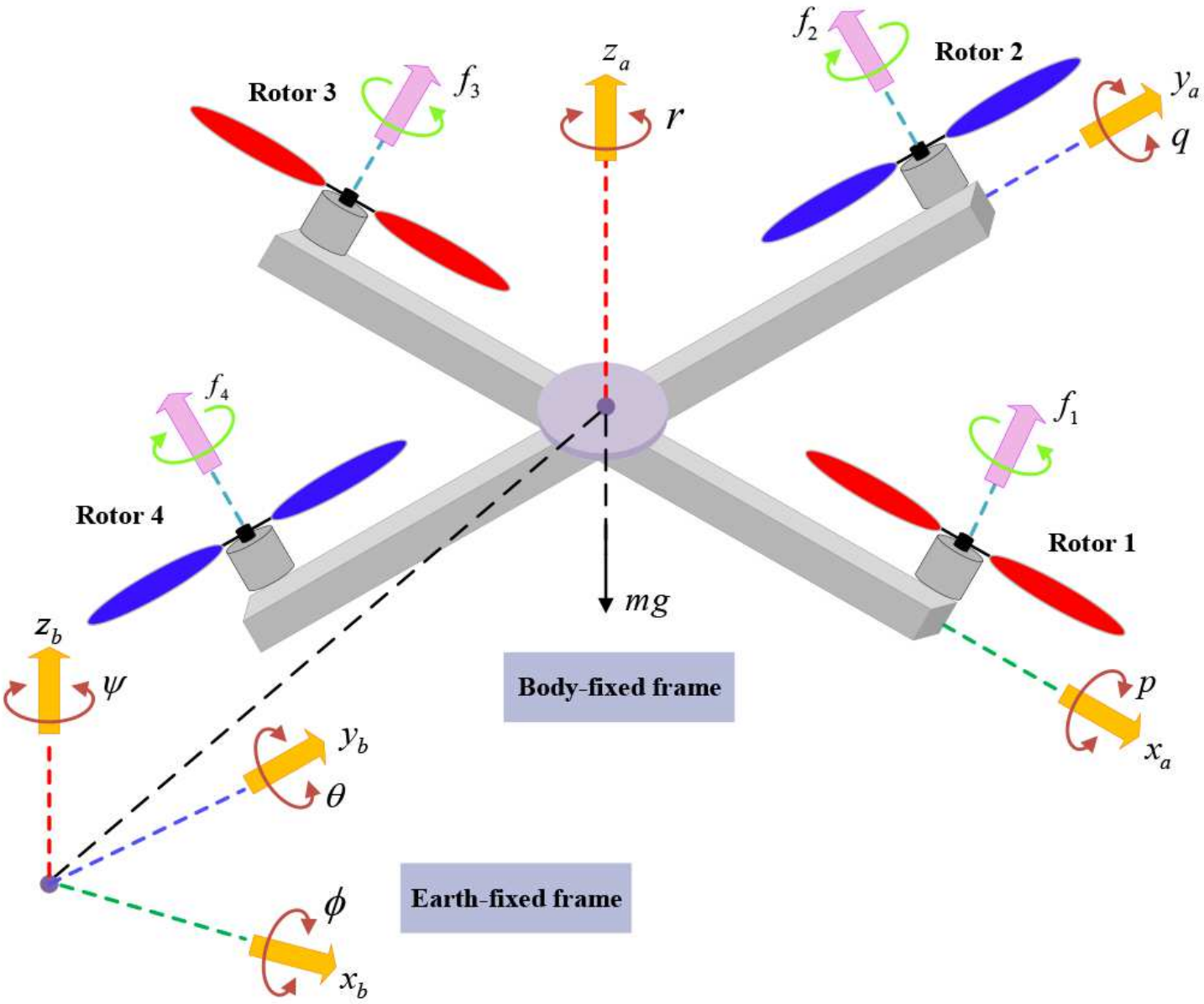

Figure 1

Schematic conguration of a quadrotor UAV.

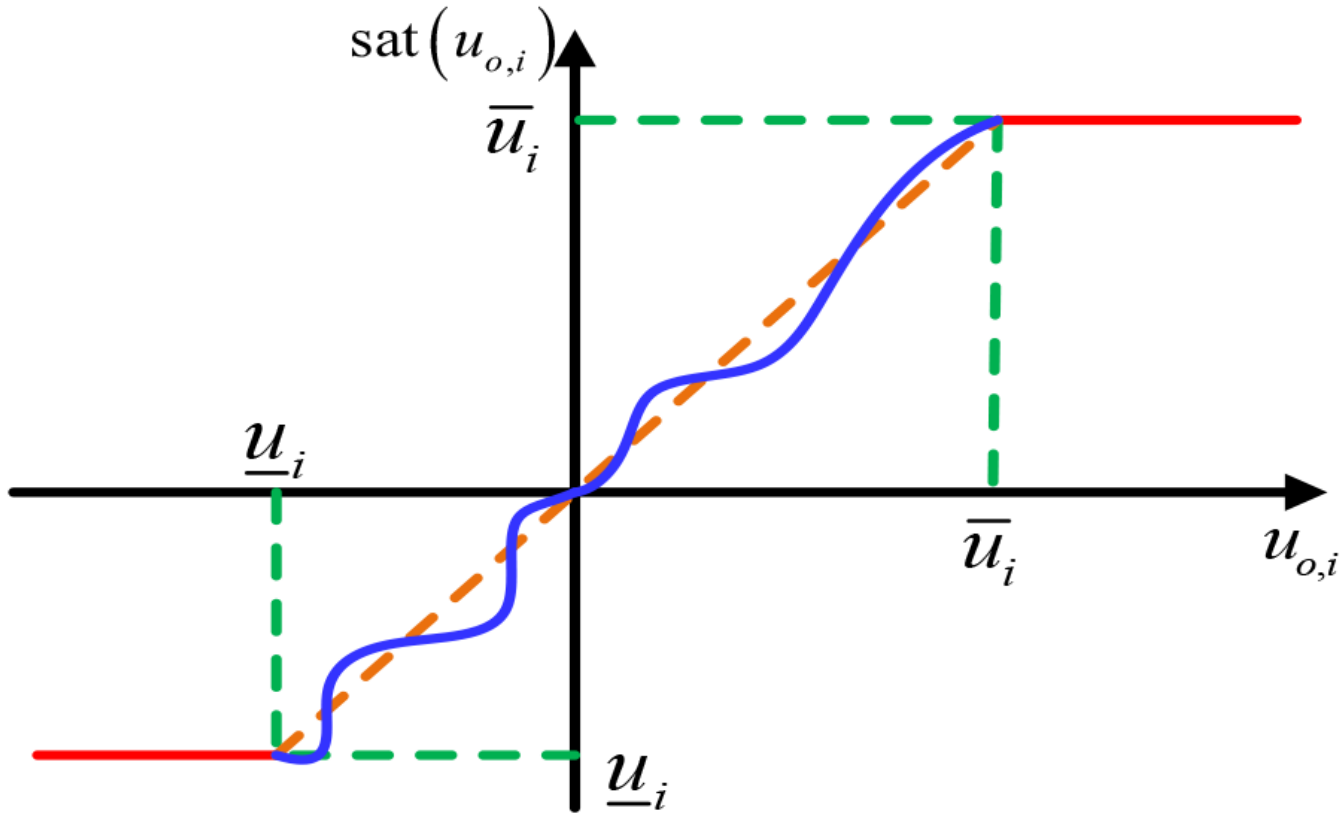

Figure 2

Non-symmetric input saturation.

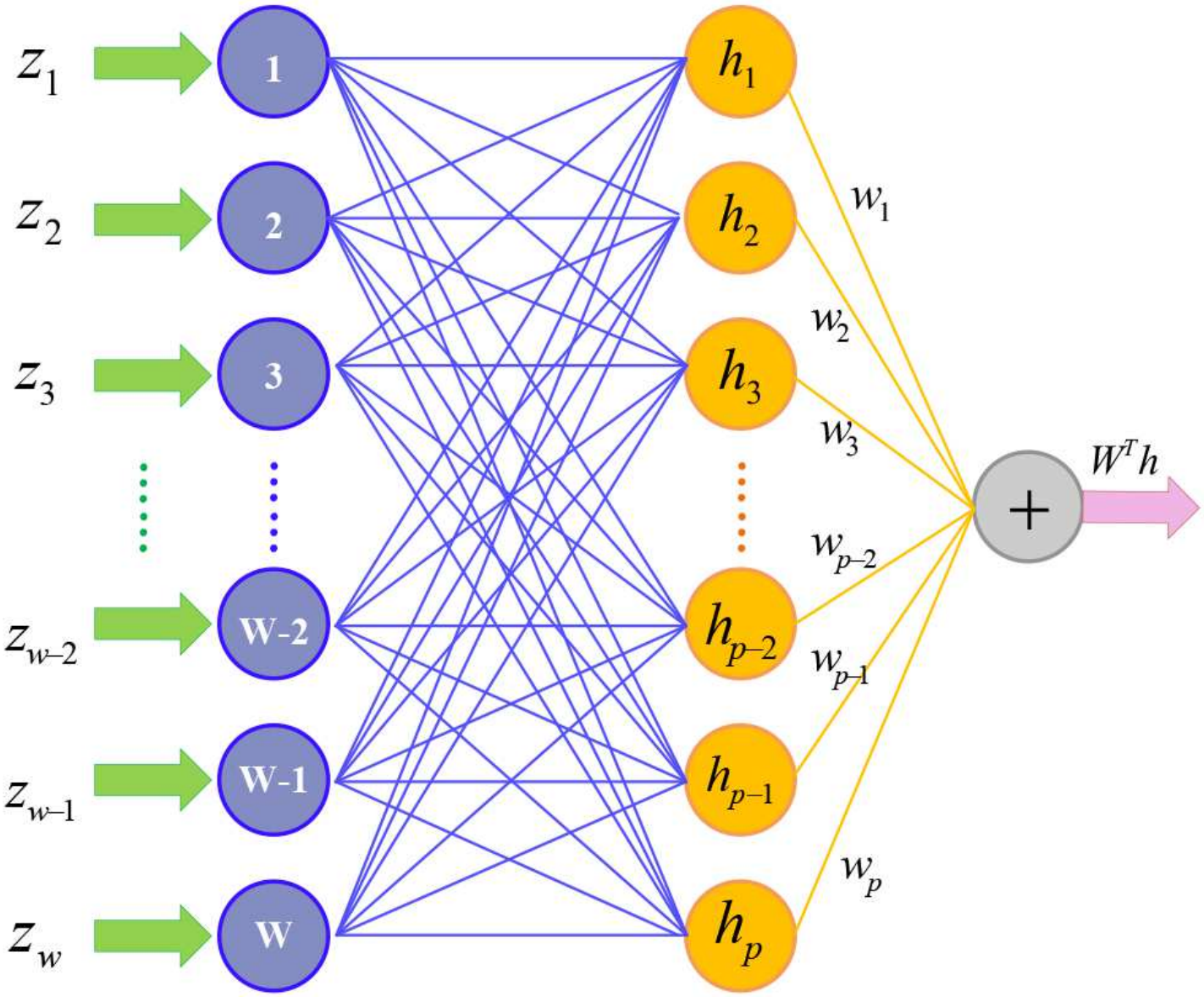

Figure 3

Description of the architecture of the RBFNN used in this study, where the grey circle is the output of the RBFNN, the orange circle is the output of the hidden layer, and the blue circle is the input of the RBFNN.

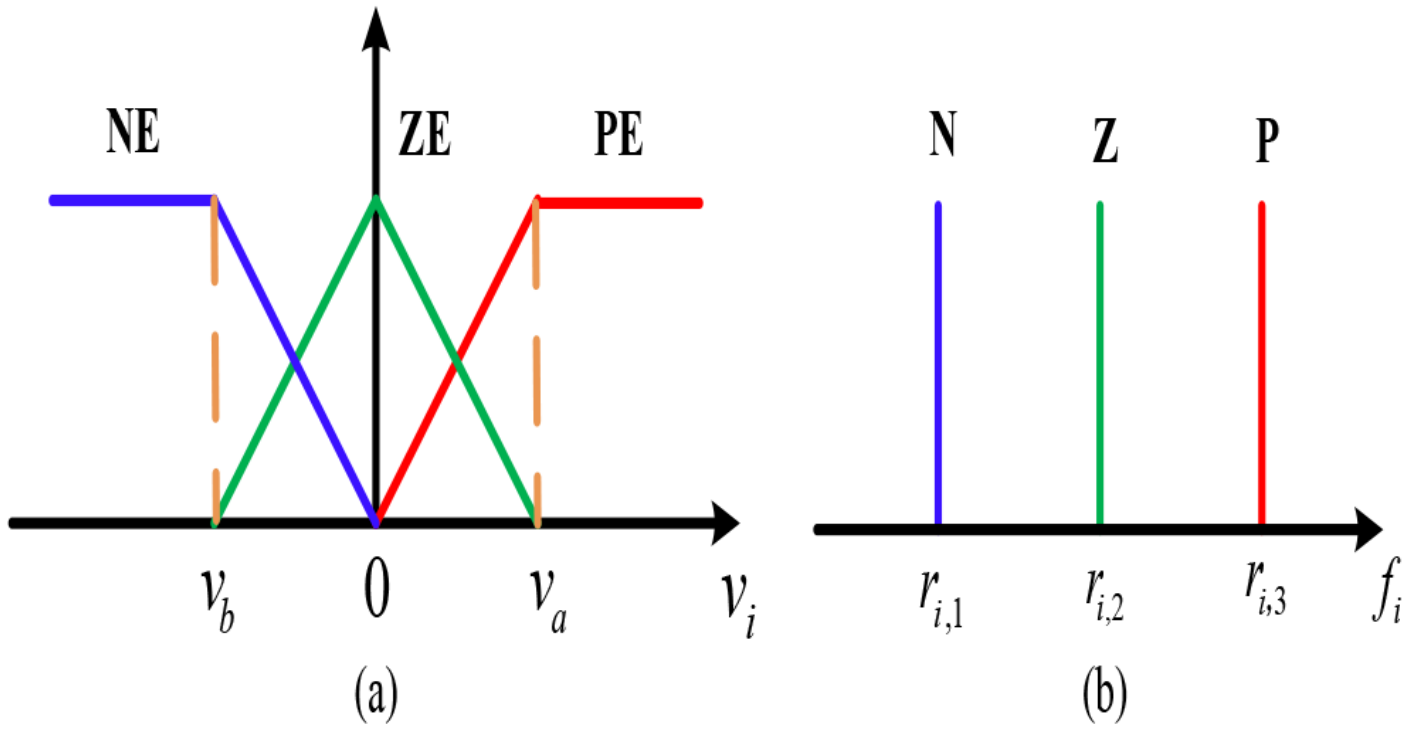

Figure 4

Membership functions. (a) Input fuzzy sets for vi; (b) Output fuzzy sets for fi.

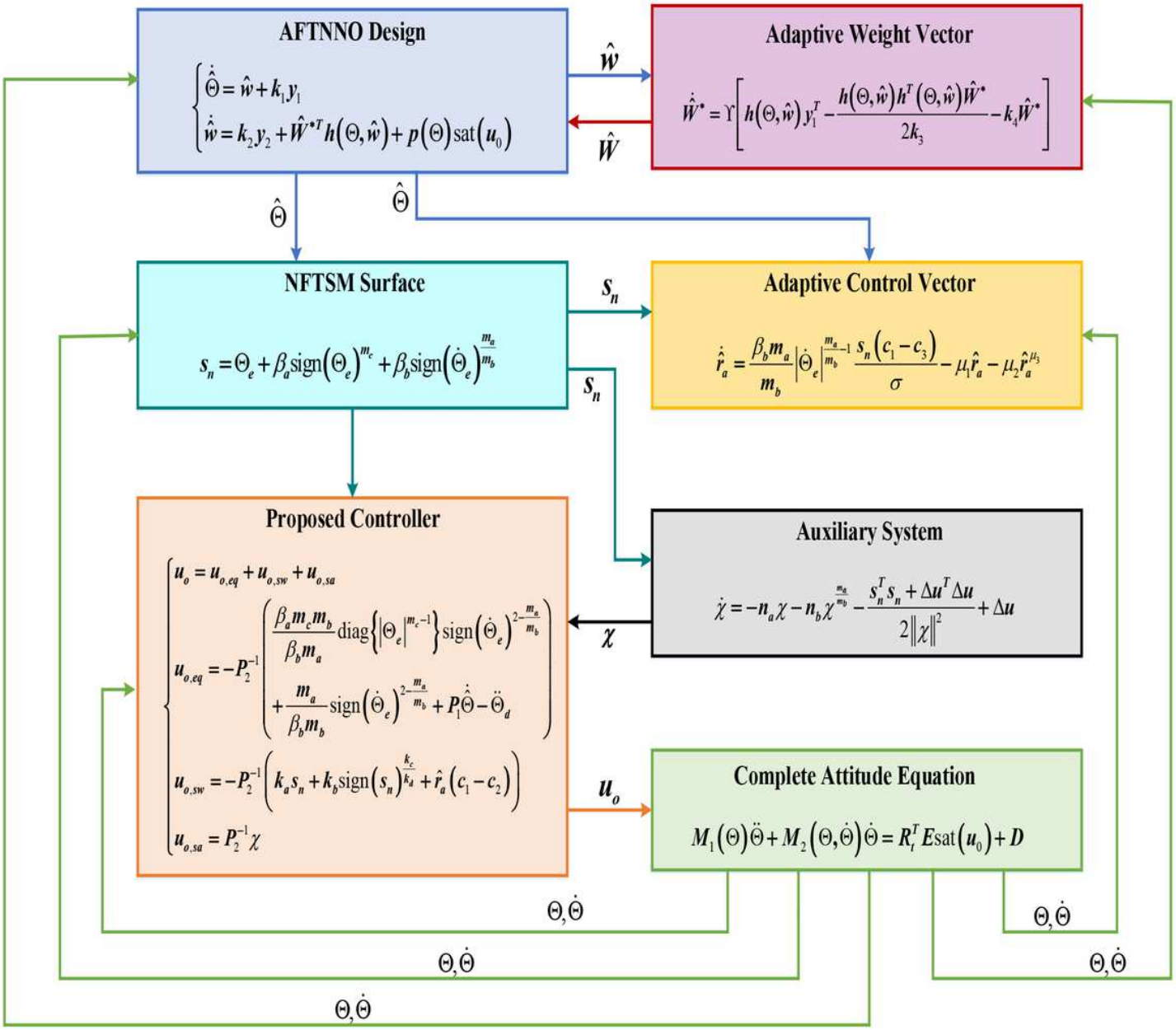

Figure 5

Block diagram of the proposed control scheme

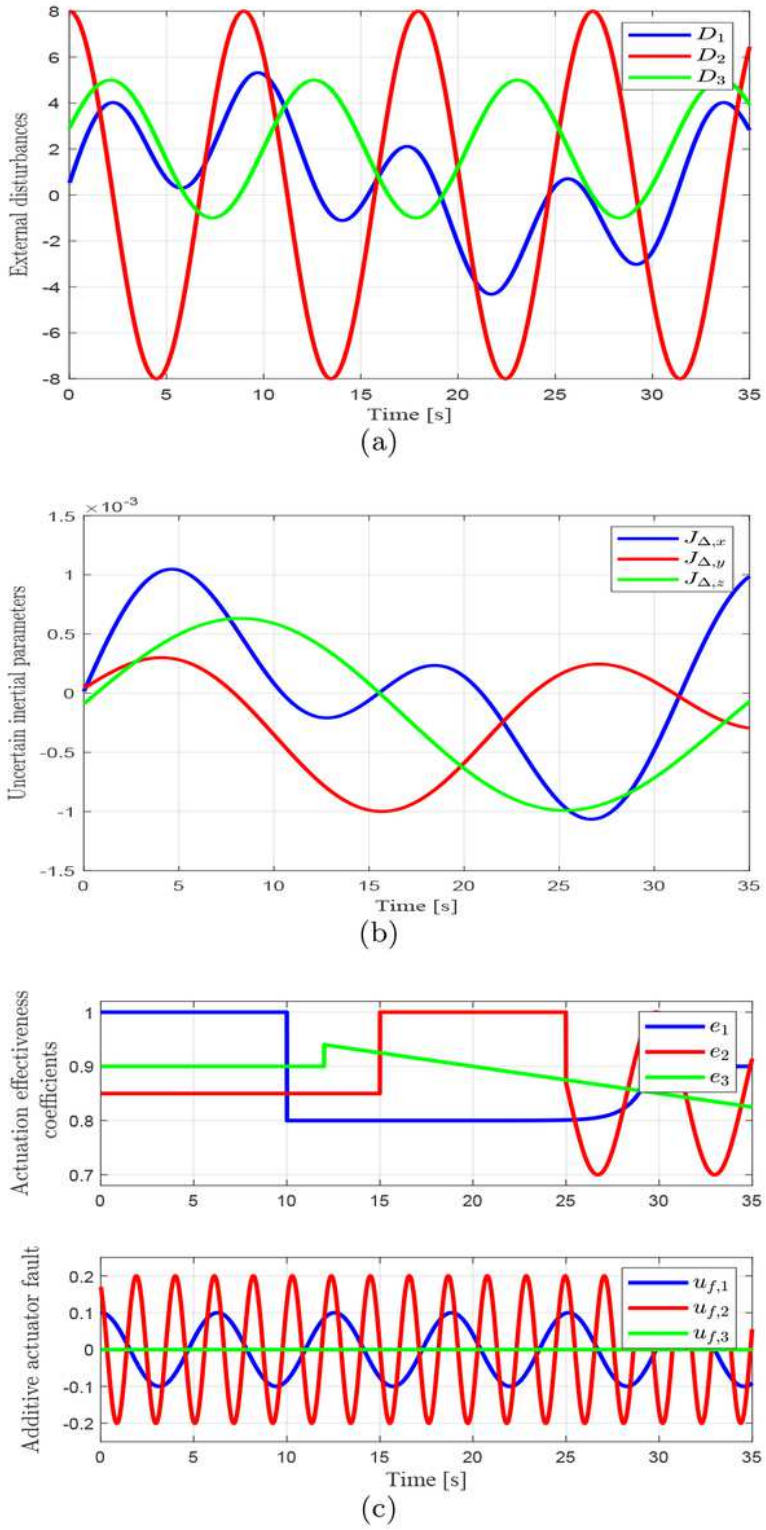

Figure 6

Time response of the attitude angle.

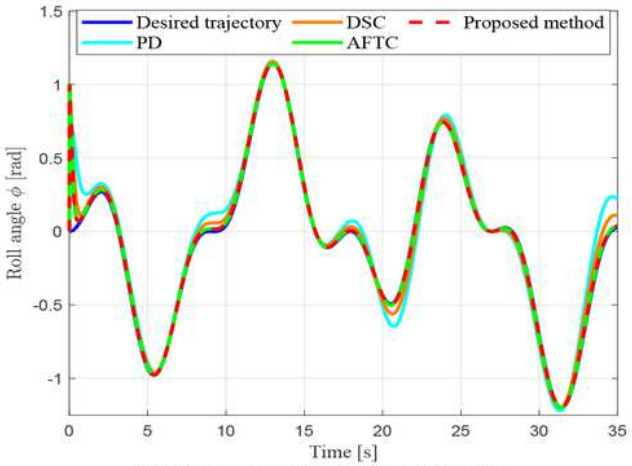

(a) Time response of the roll angle

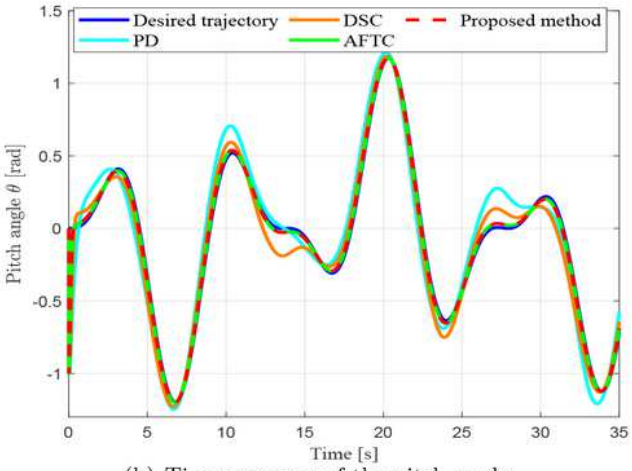

(b) Time response of the pitch angle

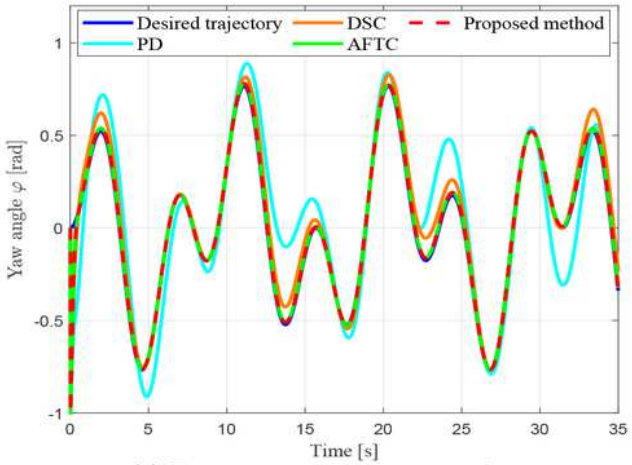

(c) Time response of the yaw angle

Figure 7

Time response of the attitude angle.

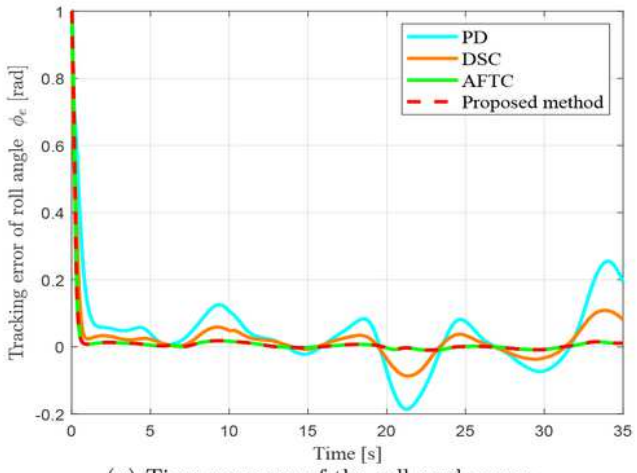

(a) Time response of the roll angle error

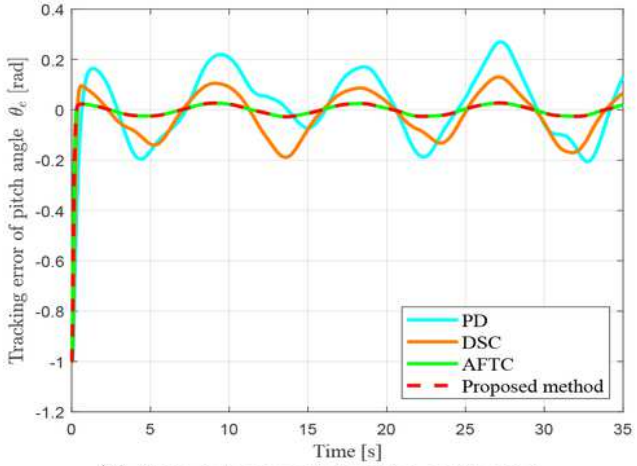

(b) Time response of the pitch angle error

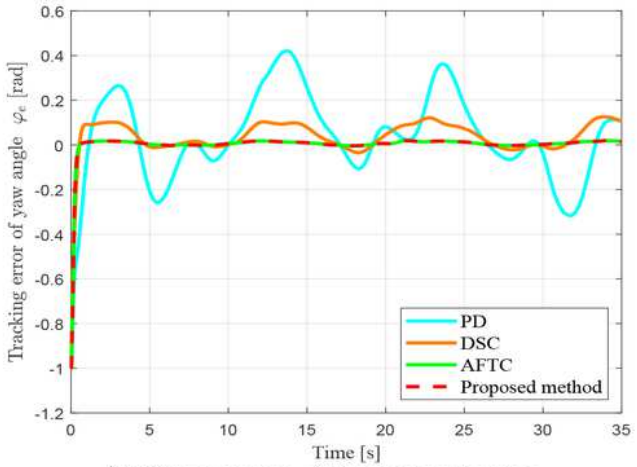

(c) Time response of the yaw angle error

Figure 8

Time response of the attitude angle error.

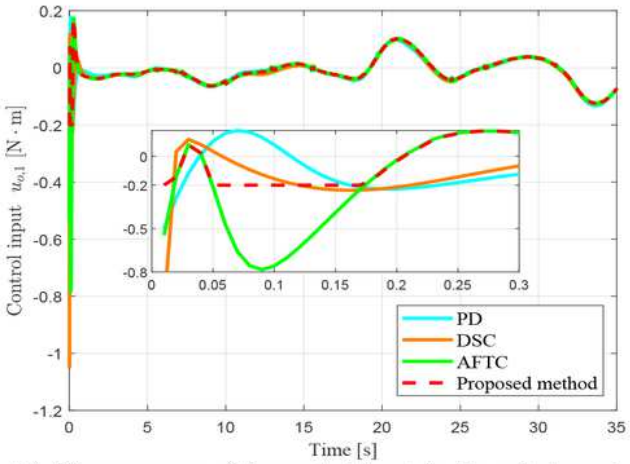

(a) Time response of the control input in the roll channel

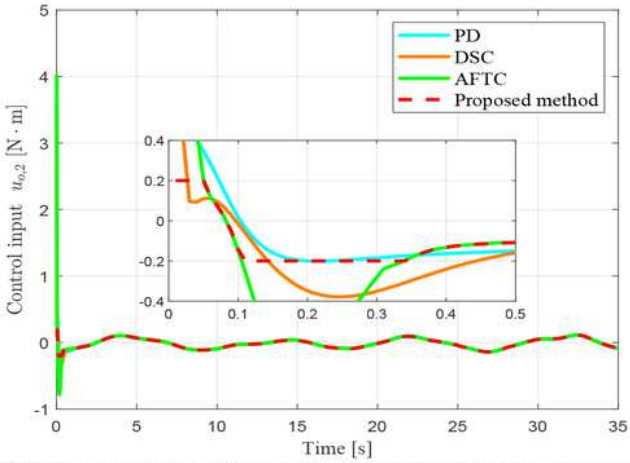

(b) Time response of the control input in the pitch channel

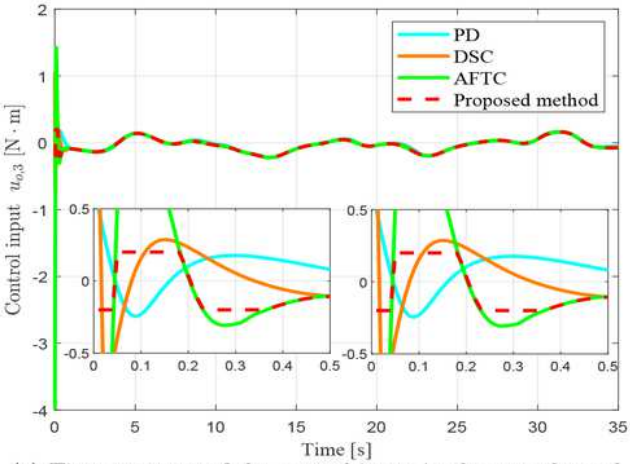

(c) Time response of the control input in the yaw channel

Figure 9

Time response of the control input.

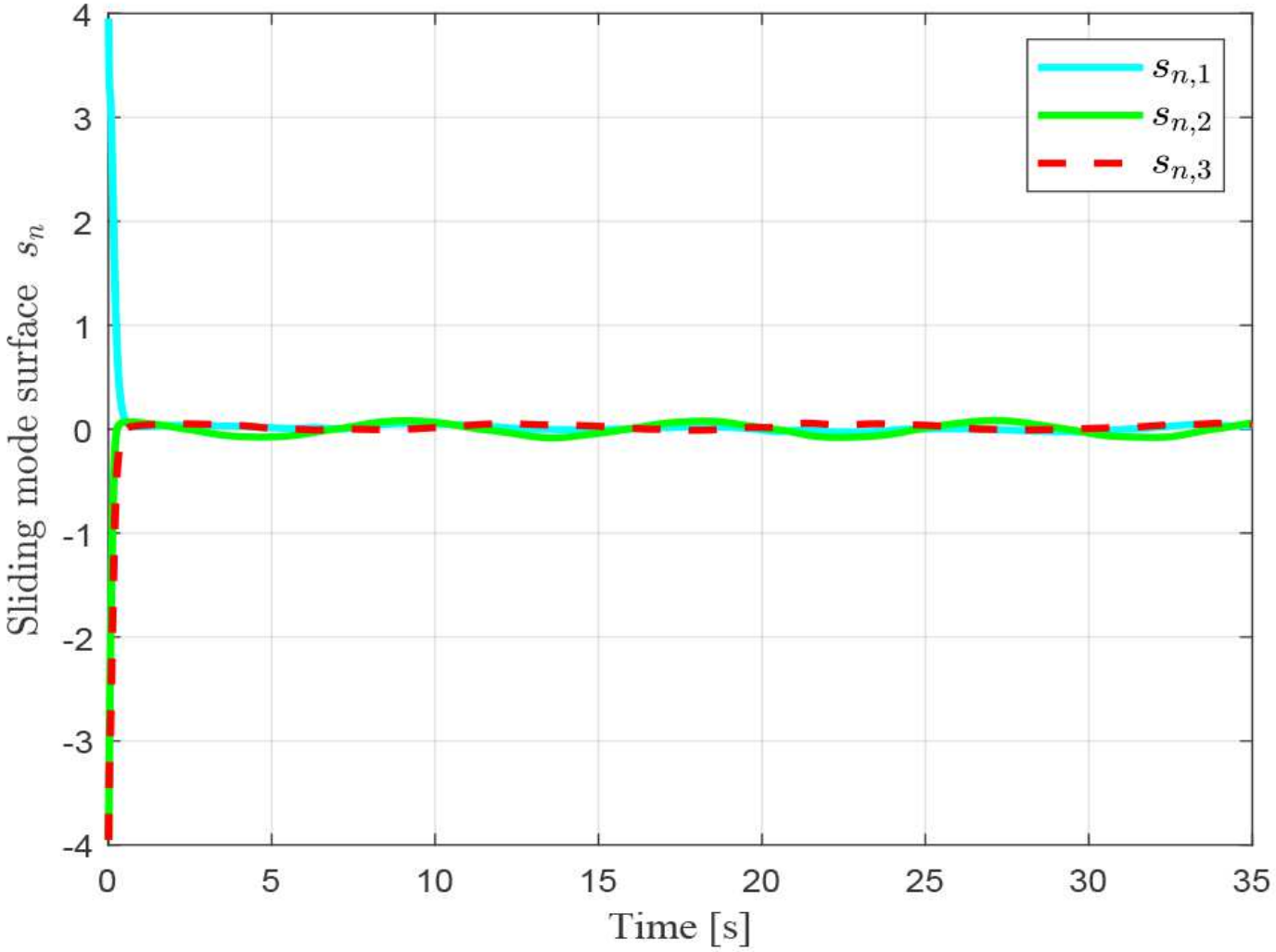

Figure 10

Time response of sliding mode surface under the proposed controller.

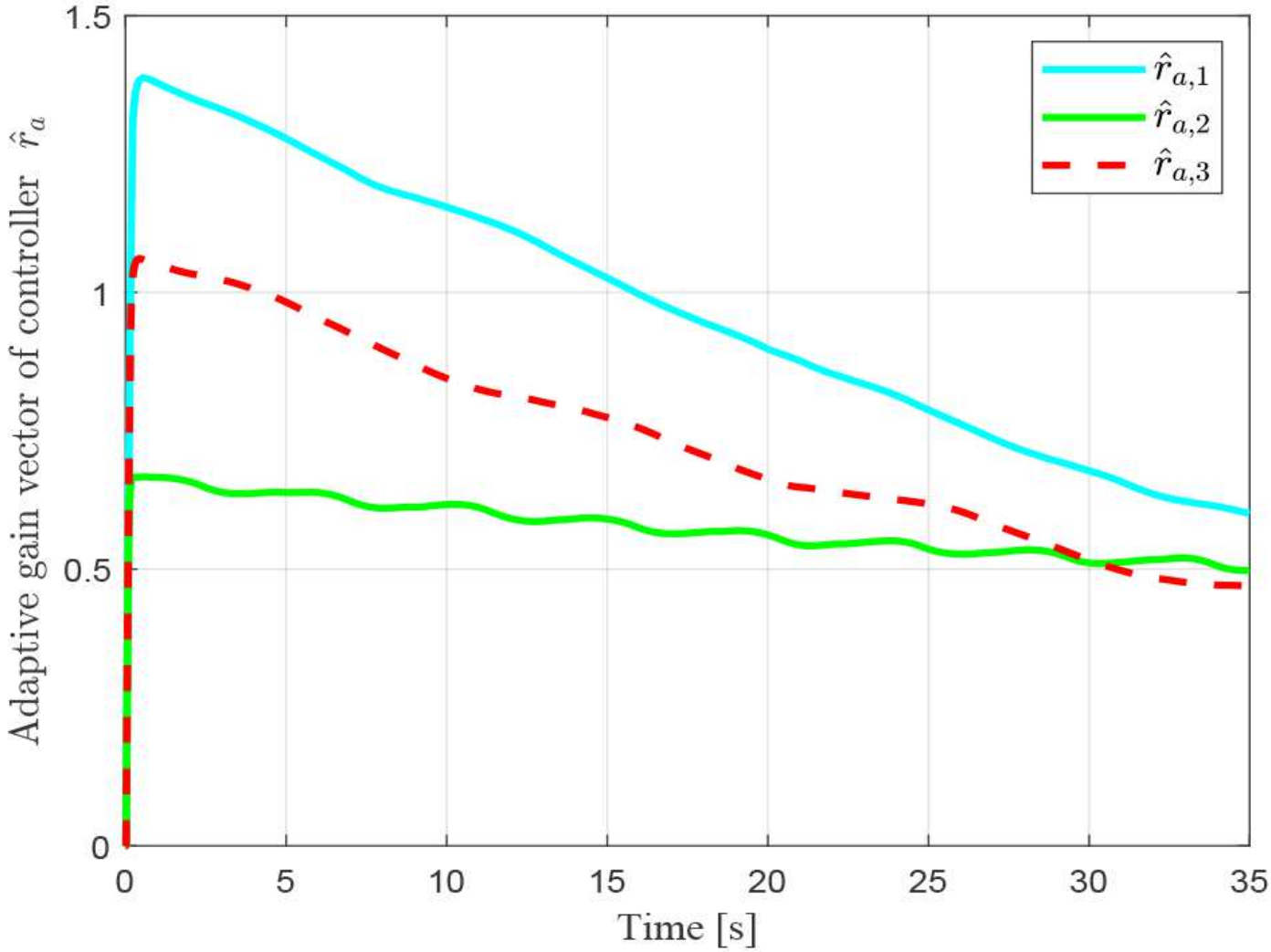

Figure 11

Time response of adaptive gain vector under the proposed controller.

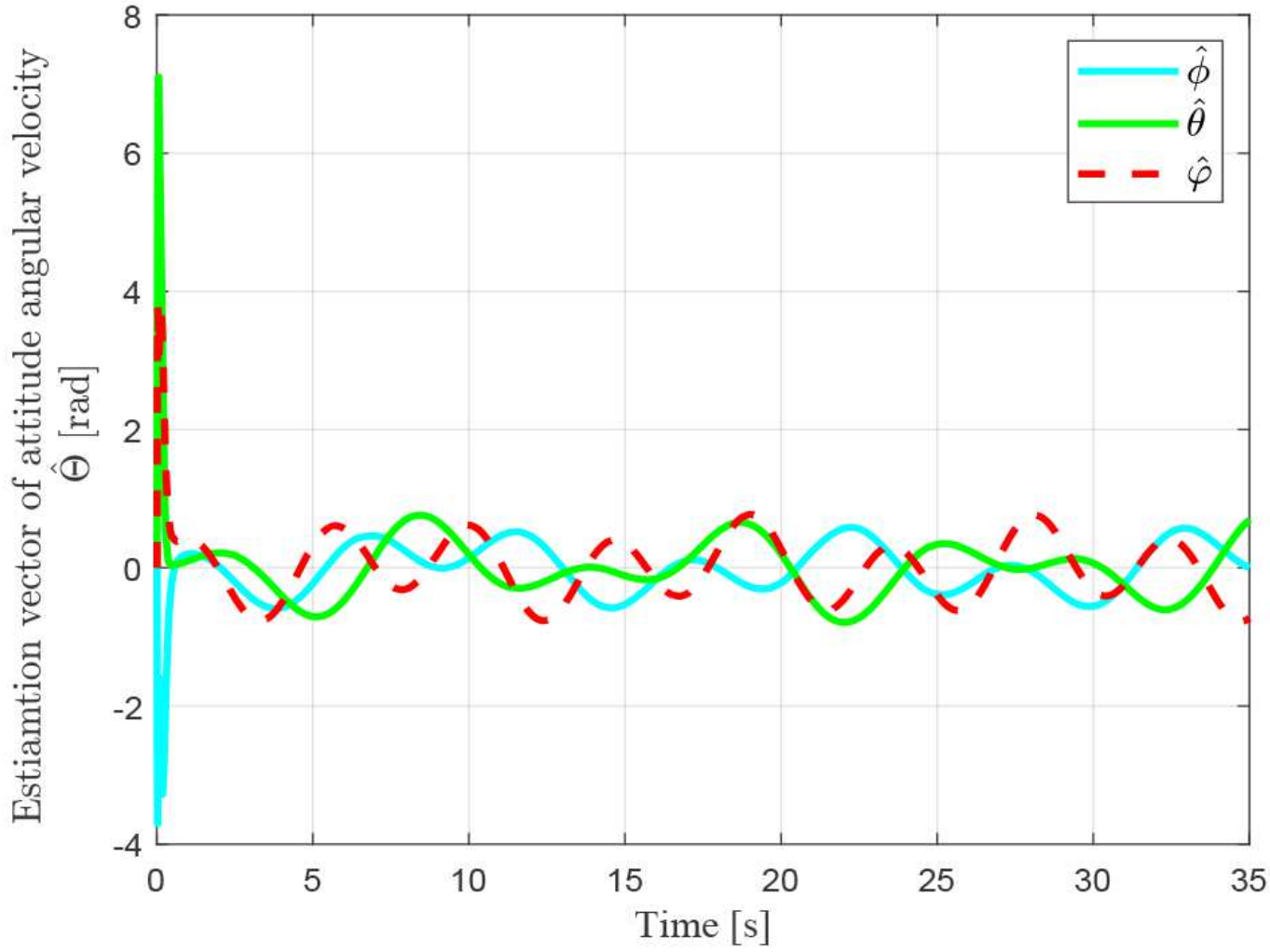

Figure 12

Time response of the estimation for the attitude angular velocity.

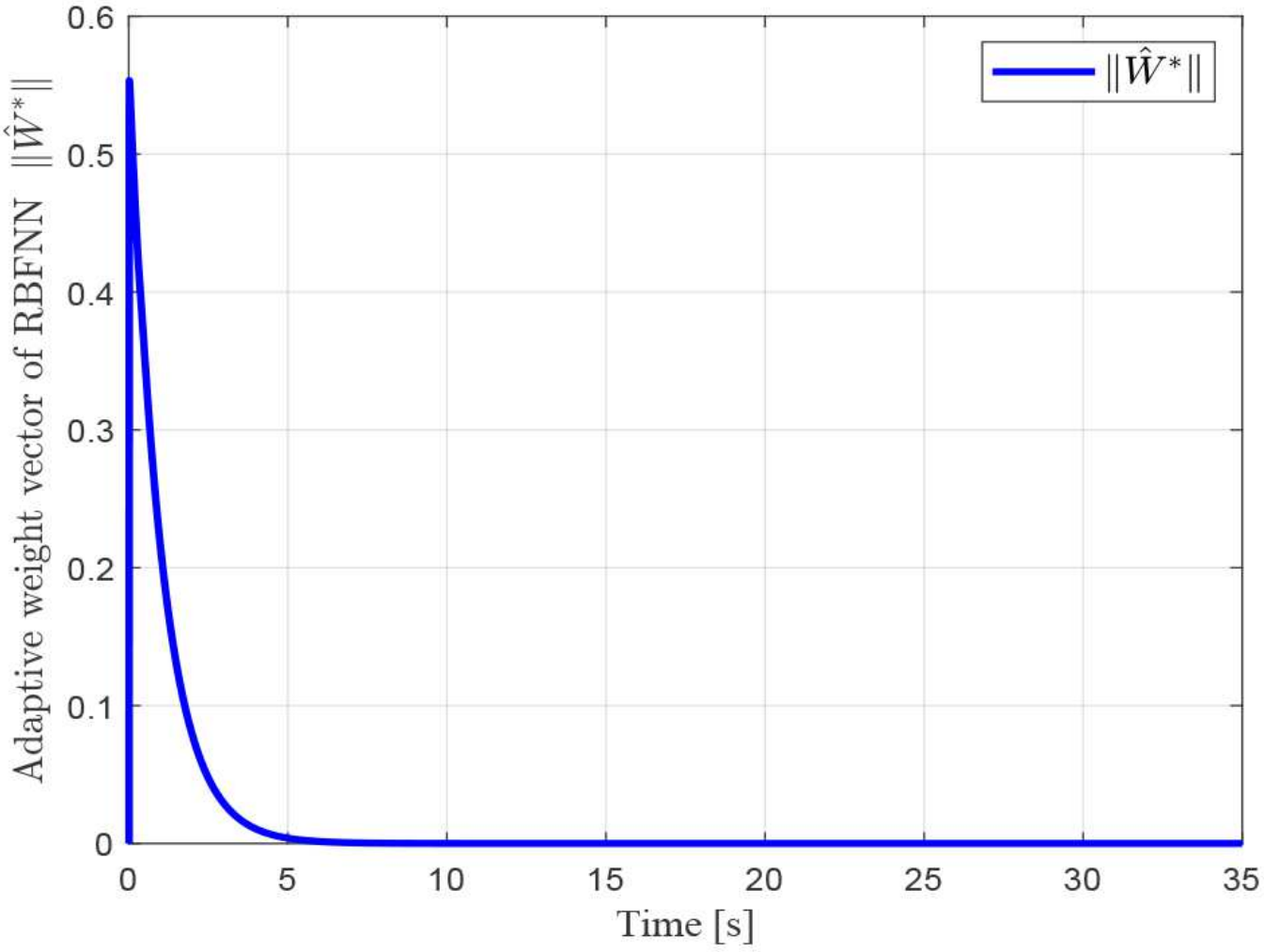

Figure 13

Time response of adaptive weight in the RBFNN.

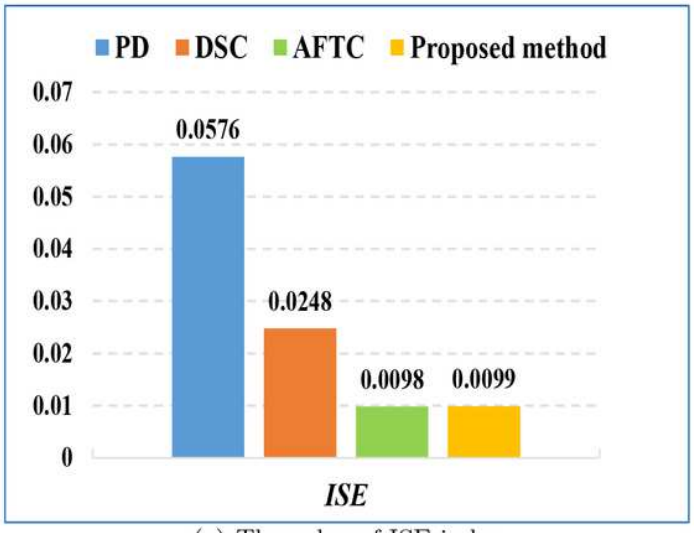

(a) The value of ISE index

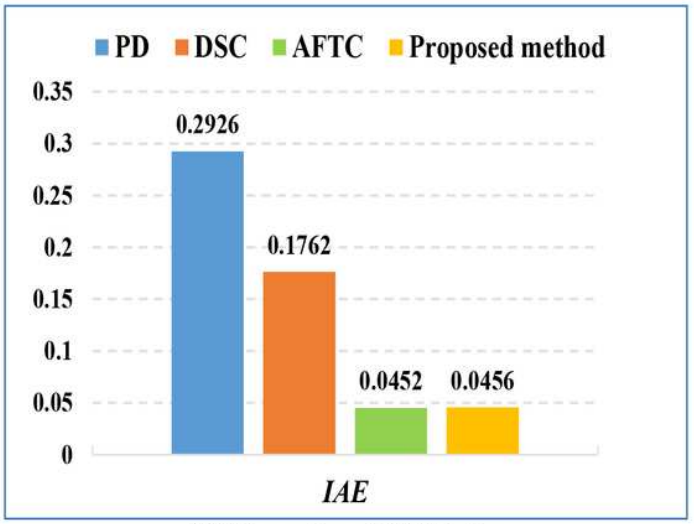

(b) The value of IAE index

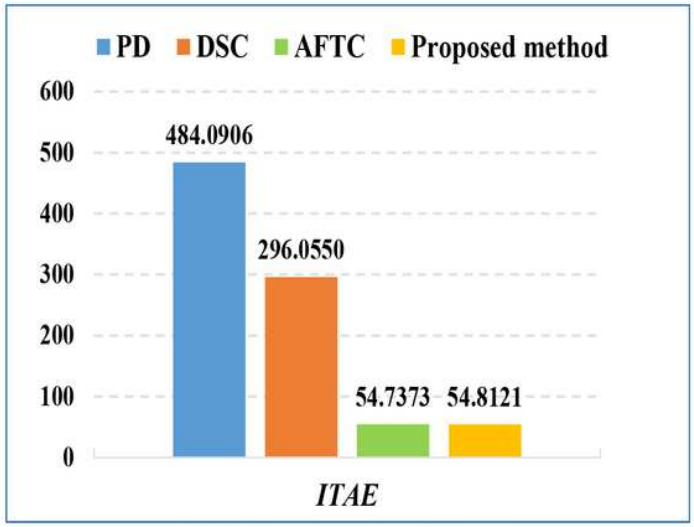

(c) The value of ITAE index

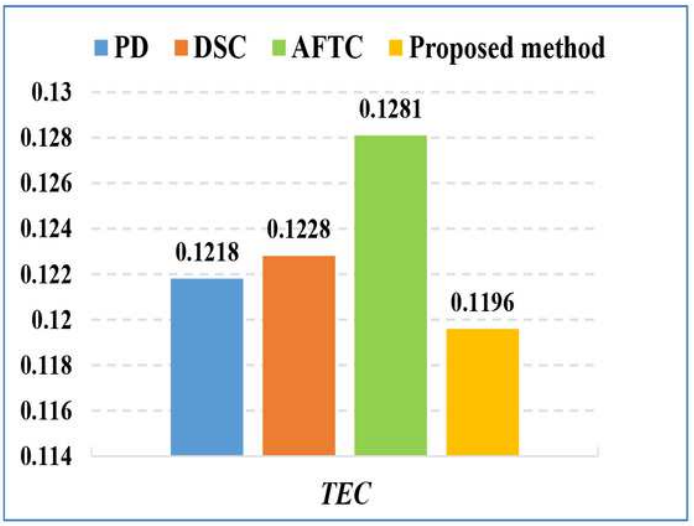

(d) The value of TEC index

Figure 14

Comparison of performance index values.